FINAL REPORT

Estimating Oil Slick Thickness with LiDAR Remote Sensing Technology

Submitted to:

Bureau of Safety and Environmental Enforcement (BSEE)
Oil Spill Response Research Branch

Submitted by:

U.S. Naval Research Laboratory
4555 Overlook Ave., SW
Washington, DC 20375

29 March 2019

Acknowledgments

This report is part of a study that was funded by the United States Bureau of Safety and Environmental Enforcement (BSEE), Department of the Interior (DOI), Washington, D.C., under Contract Number E17PG00038.

Disclaimer

This report is part of a study that was funded by the United States Bureau of Safety and Environmental Enforcement (BSEE), Department of the Interior (DOI), Washington, D.C., under Contract Number E17PG00038.

Estimating Oil Slick Thickness with LiDAR Remote Sensing Technology

Final Report to:
Bureau of Safety and Environmental Enforcement (BSEE)
Interagency Agreement number E17PG00038
March 2019

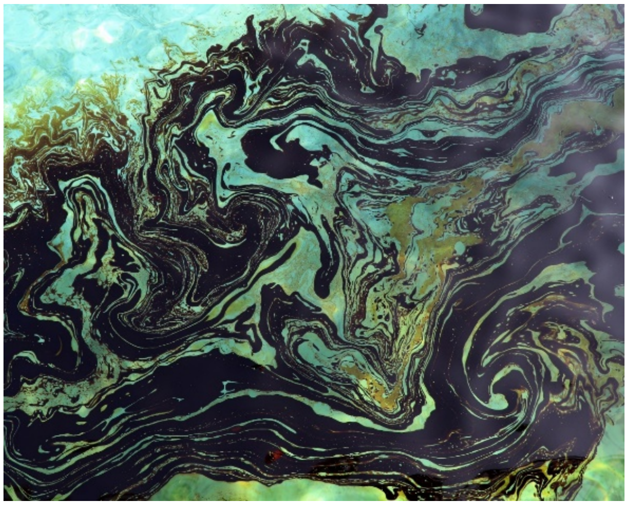

Richard W. Gould, Jr.*, Ph.D.
U.S. Naval Research Laboratory
Bio-Optical/Physical Processes and Remote Sensing, Code 7331
Stennis Space Center, MS 39529
Tel: 228-688-5587, Fax: 228-688-4149, Email: richard.gould@nrlssc.navy.mil
**Correspondence*

Damien Josset, Ph.D.
U.S. Naval Research Laboratory
Ocean Hydro Optics, Sensors and Systems, Code 7333
Stennis Space Center, MS 39529
Tel: 228-688-4408, Fax: 228-688-4149, Email: damien.josset@nrlssc.navy.mil

Stephanie Anderson
U.S. Naval Research Laboratory
Bio-Optical/Physical Processes and Remote Sensing, Code 7331
Stennis Space Center, MS 39529
Tel: 228-688-5264, Fax: 228-688-4149, Email: stephanie.anderson@nrlssc.navy.mil

Wesley Goode
U.S. Naval Research Laboratory
Ocean Hydro Optics, Sensors and Systems, Code 7333
Stennis Space Center, MS 39529
Tel: 228-688-5265, Fax: 228-688-4149, Email: wesley.goode@nrlssc.navy.mil

Robyn N. Conmy, Ph.D.
U.S. Environmental Protection Agency ORD
National Risk Management Research Laboratory LRPCD
26 W. Martin Luther King Drive, Cincinnati, OH 45268
Tel: 513-569-7090, Fax: 513-569-7620, Email: conmy.robyn@epa.gov

Blake Schaeffer, Ph.D.
U.S. Environmental Protection Agency ORD
National Exposure Research Laboratory
109 T.W. Alexander Dr., Research Triangle Park, NC 27711
Tel: 919-541-5571, Fax: 919-541-0160, Email: schaeffer.blake@epa.gov

Steve Pearce, Ph.D.
ASL Environmental Sciences, Inc.
#1-6703 Rajpur Place
Victoria, BC, V8M 1Z5 Canada
Tel: 250-656-0177 (x150), Toll Free: 1-877-656-0177, Email: spearce@aslenv.com

Todd Mudge
ASL Environmental Sciences, Inc.
#1-6703 Rajpur Place
Victoria, BC, V8M 1Z5 Canada
Tel: 250-656-0177 (x116), Toll Free: 1-877-656-0177, Email: tmudge@aslenv.com

James Bartlett
ASL Environmental Sciences, Inc.
#1-6703 Rajpur Place
Victoria, BC, V8M 1Z5 Canada
Tel: 250-656-0177 (x153), Toll Free: 1-877-656-0177, Email: jbartlett@aslenv.com

David Lemon
ASL Environmental Sciences, Inc.
#1-6703 Rajpur Place
Victoria, BC, V8M 1Z5 Canada
Tel: 250-656-0177 (x122), Toll Free: 1-877-656-0177, Email: dlemon@aslenv.com

Dave Billenness
ASL Environmental Sciences, Inc.
#1-6703 Rajpur Place
Victoria, BC, V8M 1Z5 Canada
Tel: 250-656-0177 (x126), Toll Free: 1-877-656-0177, Email: dbillenness@aslenv.com

Oscar Garcia, Ph.D.
Water Mapping, LLC.
3010 Coral Strip Parkway, Gulf Breeze, FL 32563
Tel: 361-244-6575, Email: oscar.garcia@watermapping.com

1. EXECUTIVE SUMMARY

The ability to characterize oil spills using pulsed laser light (Light Detection And Ranging - LiDAR) technology is in its infancy. To more fully explore and capitalize on this technology, a team of researchers from the U.S. Naval Research Laboratory at the Stennis Space Center (NRL/SSC), the U.S. Environmental Protection Agency (EPA), and ASL Environmental Sciences collected a multidisciplinary data set in July 2018 at the National Oil Spill Response Research & Renewable Energy Test Facility (Ohmsett) in Leonardo, NJ. During controlled surface and subsurface oil release experiments, an extensive suite of LiDAR, optical, acoustic, thermal, and chemical data sets were collected, to assess how these signals change as a function of oil thickness and type. Specifically, our primary goals were to evaluate LiDAR backscattering intensity (strength of the return signal from the various oil types, and oil/emulsion thicknesses), fluorescence intensity, and polarization. Secondarily, we sought to develop and validate new measurement protocols and new algorithms, using LiDAR, optical, and acoustic data sets, individually and in combination, to differentiate oil types and estimate oil thicknesses. The acoustic transducers (AZFP) detected the subsurface oil release at all four frequencies, and the signal-to-noise ratio was in excess of 50 dB for each AZFP channel. Initial results from this experiment indicate that the oil is clearly detectable by the AZFP, and that longer-range detection is likely possible. LiDAR remote sensing can detect and measure the presence of oil at the surface or underwater, and can retrieve a wide range of oil thickness, from a few microns up to several mm thick. In addition, fluorescence provides an unambiguous signature of the presence of oil.

2. INTRODUCTION

When crude and fuel oils are released into the environment, information on the spatial extent, slick thickness and emulsification state is crucial for operational decision-making during an oil spill. Combined, these variables describe the amount of spilled oil present and its weathering state. This in turn determines how oil moves on the sea surface or mixes into a water column. They also provide information on ‘actionable oil’ and influence the allocation of spill response resources and countermeasure options (vessels, booms, skimmers, recovery, in situ burning). Obtaining spatial extent or surface expression of oil slicks can be accomplished in a variety of ways with fairly good certainty. This can be accomplished via visual confirmation from aerial surveys or ship. Presence of slicks can also be determined by aerial surveys with instrumentation such as cameras and pushbroom scanners, laser fluorosensors, active microwave sensors like Synthetic Aperture Radar (SAR), and multispectral/hyperspectral visible, near-IR and thermal IR sensors (Lennon et al. 2006; Lennon et al. 2005). For largest spatial coverage, space-based sensors also provide geographical extent, such as ocean color (Hu et al. 2018), SAR, and thermal IR imagery. A variety of passive and active airborne and satellite sensors and analysis techniques are summarized in recent reviews (Brekke and Solberg 2005; Fingas and Brown 2014; Leifer et al. 2012).

Obtaining slick thickness, however, comes with greater challenges, where reliable measures of thickness are a knowledge gap (Fingas 2018). Slick thickness measurements are difficult and in their infancy (Fingas and Brown 2014). For visual observations, the relationship between oil appearance and thickness is widely used, where minimum visible thickness is roughly 0.1 µm. In the 1970's Hornstein (1973) correlated a threshold of rainbow colors to thickness, and classifications for sheen through thicker oil were defined by color. Microwave radiometry was used to delineate thickness, where sheens were found to be 2-4 µm thick (Hollinger and Mennella 1973) and that 90% of spilled oil was located in only10% of area, indicating the immense patchiness of slicks. This early research is still used today and is the basis for the NOAA Observer Job Aid oil classification, which characterizes oil based on appearance from sheen to dark oil and assigns relative thickness. Yet, these approaches are subjective and cannot offer estimates of oil thickness above a few millimeters and there are issues with false positives (red tide, kelp, seagrass, fish schools, etc).

In recent years, there have been a number of studies dedicated to improving thickness measurements. Ultra-violet (UV) and infra-red (IR) sensors used in concert have been shown to provide thickness estimates based on temperature and reflectivity indices (Zielinski et al. 2001). Coincident SAR, multispectral visible-near IR and thermal IR have also shown promise. Svejkovsky et al. (2012) and Svejkovsky et al. (2016) demonstrated that by measuring the visible and thermal reflectance signatures of oil layers of varying thicknesses and applying reflectance ratio algorithms, they could assign image pixels to oil thicknesses classes.

LiDAR is based on the differential time-of-flight of light pulses and often is used for topographic and bathymetric mapping, and subsurface ocean layer detection, but this technology also offers promise for oil spill applications. LiDAR can detect backscatter from water-column scatterers, discerning fish schools from phytoplankton layers (Carrera et al. 2006). The use of LiDAR to detect subsurface ocean layers using both airborne and satellite LiDAR systems has been demonstrated (Churnside et al. 2013; Churnside and Donaghay 2009), and Churnside (2014) provides a review of oceanographic LiDAR applications.

LiDAR systems integrated with hyperspectral sensors (such as CHARTS airborne sensor) have been shown to detect both submerged and surface oil due to transit time of bathymetric laser pulse returns, and reflective and absorptive layers that can be identified (Leifer et al. 2012). Data showed evidence of unique LiDAR return backscatter properties associated with surface oil slick features (i.e., green band, 532 nm). Spaceborne and airborne LiDAR systems (such as CALIOP and HSRL, respectively) demonstrated shallow subsurface oil during DWH (Leifer et al. 2012), but have yet to be utilized fully and require additional work to take further advantage of their potential capabilities. LiDAR systems can be deployed on in-water platforms, just above the sea surface from vessels, or from aircraft and satellites. This makes it a versatile measurement for many types of spills in a variety of regions.

We utilized the National Oil Spill Response Research and Renewable Energy Test Facility (Ohmsett) wave tank at the Naval Weapons Station Earle in Leonardo, NJ, as a testbed to assess the capability of LiDAR technology to characterize oil spills and to develop measurement protocols. The Ohmsett wave tank offers a unique capability to characterize simulated oil spills under controlled conditions, as a proxy for uncontained, natural spills in the environments. Ohmsett's above ground concrete test tank measures 203 m long by 20 m wide by 2.4 m deep and is filled with 2.6 million gallons of clear saltwater (Figure 1A). In addition, meteorological data, water temperature and salinity, and oil/water ratios can be controlled or measured. Two moveable bridges across the tank can traverse the tank lengthwise along a rail system (Figure

1B); the bridges can be coupled to move together, or de-coupled to move separately. Instruments can be attached to the bridges, either directly above the water for surface oil slick measurements, or submerged for subsurface oil measurements. A variety of oils are available for testing, as are blending tanks with a water and oil distribution system to produce custom oil/water emulsions for testing. The power and weight capacity of the bridge were adequate for operation of the NRL LiDAR systems.

NRL deployed two above-water LiDAR systems on the moveable auxiliary bridge at the Ohmsett tank facility, to measure backscatter signals from non-oiled and oiled water surfaces, using several types of oils at various thicknesses. The LiDAR systems are the Ship LiDAR Optical Profiler (SLOP) and the TURBulence Ocean LiDAR (TURBOL). They are described in more detail in the Methods section below. The systems were mounted side-by-side over the railing on the bridge at the Ohmsett tank (Figure 2).

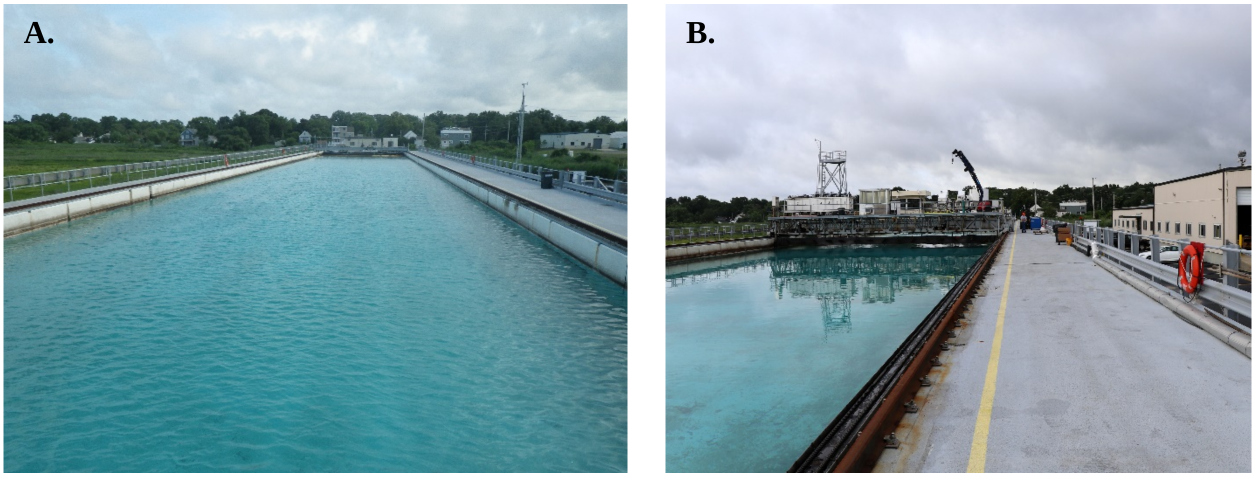

Figure 1. Ohmsett Test Tank. A. View from the main bridge, looking south. B. Moveable main and auxiliary bridges spanning the tank.

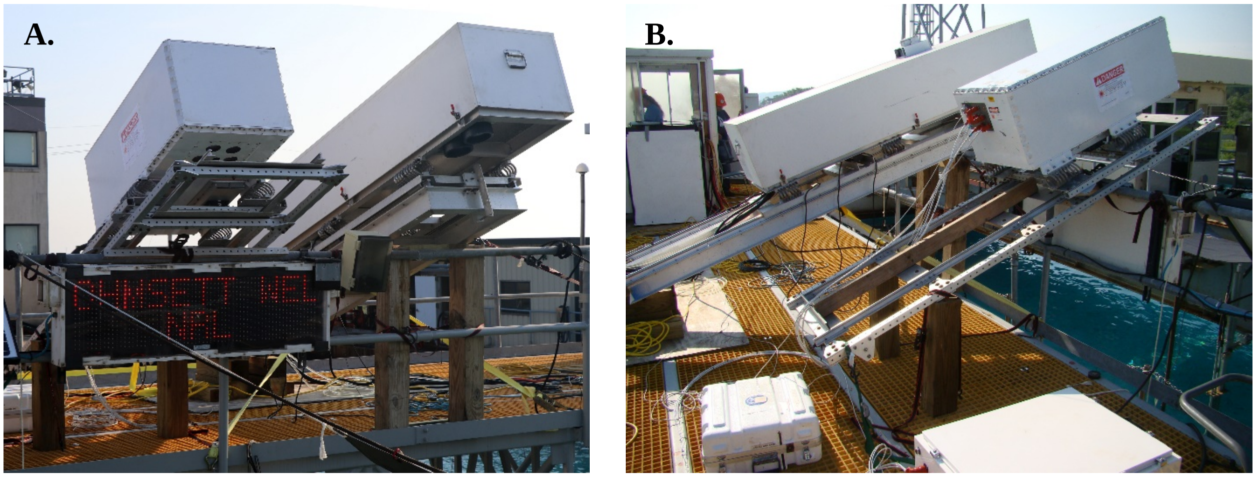

Figure 2. NRL LiDAR systems deployed on the railing on the auxiliary bridge (facing the main bridge). SLOP on the left, TURBOL on the right. A. Front view. B. Rear view.

To address critical knowledge gaps pertaining to estimates of crude oil slick thickness, the **objectives** of the work are to:

1) Evaluate above-water LiDAR technologies, in terms of backscatter signal intensity, fluorescence, and polarization, to characterize oil slicks and oil/water emulsions.
2) Develop and validate new measurement protocols and new algorithms, using LiDAR, optical, and acoustic data sets, individually and in combination, to differentiate oil types and estimate oil thicknesses.

The work was conducted by a team of researchers from the U.S. Naval Research Laboratory at the Stennis Space Center in Mississippi (NRL/SSC), and the U.S. Environmental Protection Agency (EPA) National Risk Management Research Laboratory (NRMRL, Cincinnati, OH) and National Exposure Research Laboratory (NERL, Research Triangle Park, NC). Researchers from ASL Environmental Sciences, Inc. (Canada) were involved as unfunded collaborators.

All goals have been completed. The data and analyses provide insight into the application of LiDAR technology, alone and in combination with complementary data sets, to assess surface and subsurface oil slicks and plumes. We also address "lessons learned" and make suggestions for future data collection procedures and possible additional experiments.

3. METHODS

Project partners conducted a set of experiments over a 1-week period at the Ohmsett tank. We mounted two LiDAR systems with different capabilities (described below) above the water on the moveable auxiliary bridge across the tank. We preformed both surface and subsurface oil release experiments. We created surface oil layers of varying thickness by pouring known volumes of oil into a 15-chamber floating PVC grid (5x3) with equal grid cells of known area ($1m^2$) (Figure 3A), enabling geometric calculation of oil thickness (i.e., thickness was not measured directly). However, the oil did not disperse evenly within the grid cells, particularly for the thin layers (Figures 3B), so the thickness calculations are likely inexact.

We measured HOOPS and ANS oils (crude and oil/water emulsions, provided by the Ohmsett facility) at varying thicknesses with the LiDAR, optical, and acoustic sensors. Table 1 shows the grid cell orientation, numbering convention, oil types, and oil volumes added in each grid cell. Assuming uniform oil dispersion in each grid cell, corresponding oil thicknesses for each oil volume (in parentheses) are: 0.1 mm (0.1 l), 0.5 mm (0.5 l), 1.0 mm (1.0 l), 3.0 mm (3.0 l), and 5.0 mm (5.0 l).

We collected above-water thermal imagery and fluorescence measurements from the auxiliary bridge. We also collected acoustic data using a 4-transducer acoustic sensor mounted on a pole attached to the main bridge, with the sensor head located near the bottom of the tank looking upward. We examined oil-free and oiled water areas of the tank with varying LiDAR wavelength and instrument settings (fluorescence, polarization), for both the surface and subsurface oil releases.

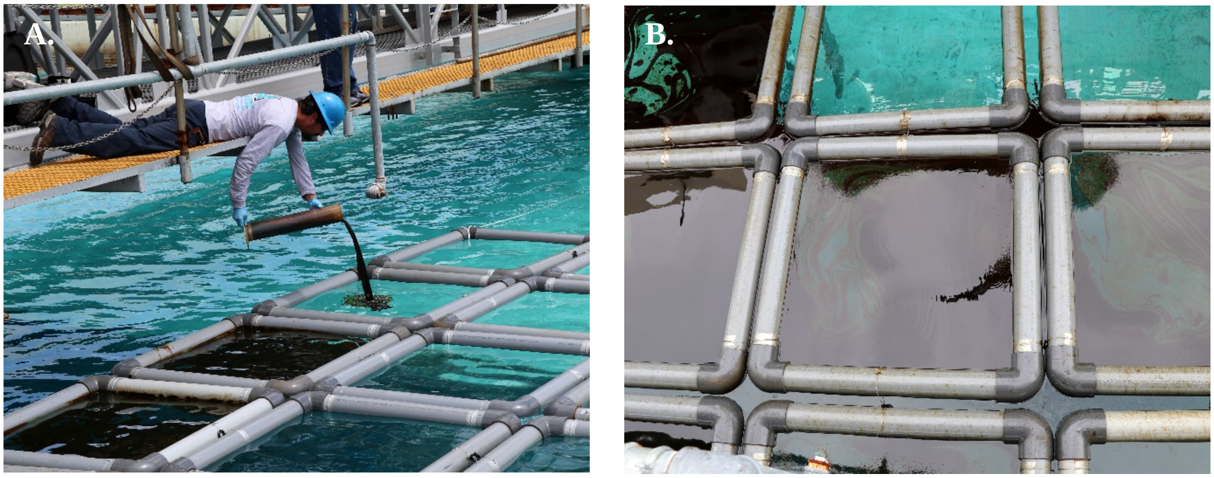

Figure 3. A. Ohmsett personnel filling 15-cell PVC grid for surface oil samples with varying oil types and thicknesses. B. Non-uniform oil dispersal in the grid cells.

Table 1. 15-chamber grid cell orientation, numbering, and oil samples.

[SOUTH – toward main bridge]

ANS 5 emulsion 5.0 liter	ANS 4 emulsion 3.0 liter	ANS 3 emulsion 1.0 liter	ANS 2 crude 1.0 liter	1 CLEAR (no oil)
HOOPS 10 emulsion 5.0 liter	HOOPS 9 emulsion 3.0 liter	HOOPS 8 emulsion 1.0 liter	HOOPS 7 emulsion 0.5 liter	HOOPS 6 emulsion 0.1 liter
HOOPS 15 crude 5.0 liter	HOOPS 14 crude 3.0 liter	HOOPS 13 crude 1.0 liter	HOOPS 12 crude 0.5 liter	HOOPS 11 crude 0.1 liter

For the subsurface oil release, we mounted an oil manifold on the main bridge, with the oil release point located approximately 1’ above the bottom of the tank. We released the oil from a single 0.02” diameter nozzle in a narrow, steady stream toward the auxiliary bridge, at a flow rate of 0.76 gallons/minute. The auxiliary and main bridges were coupled, with a separation of about 15’ in between (Figure 4A). We placed a four-frequency acoustic transducer directly beneath the oil plume, looking upward (Figure 4B). For the initial subsurface release, we collected additional downstream measurements within the oil plume (particle size and chemical analyses; Figure 5A). For the next subsurface release, we collected only LiDAR and acoustic data. For this scenario, we moved the bridges together down the tank at a speed of 0.25 knots for several minutes while releasing the oil, then stopped the bridge motion to allow the subsurface oil droplets time to rise to the surface, to simulate an ascending oil plume. This start/stop bridge translation was repeated several time. Following the oil release, we released a subsurface stream of air bubbles above the acoustic transducer, to assess acoustic differences between oil droplets and air bubbles (bubbles simulate a natural gas leak, as opposed to an oil leak; Figure 5B).

The measurement scheme enabled us to assess the capabilities of using combined LiDAR, optical, thermal, and acoustic data sets for detecting and identifying oils, measuring oil thicknesses, and assessing subsurface oil plumes. Thus, we aim to develop measurement protocols and algorithms for characterizing oil types and thicknesses.

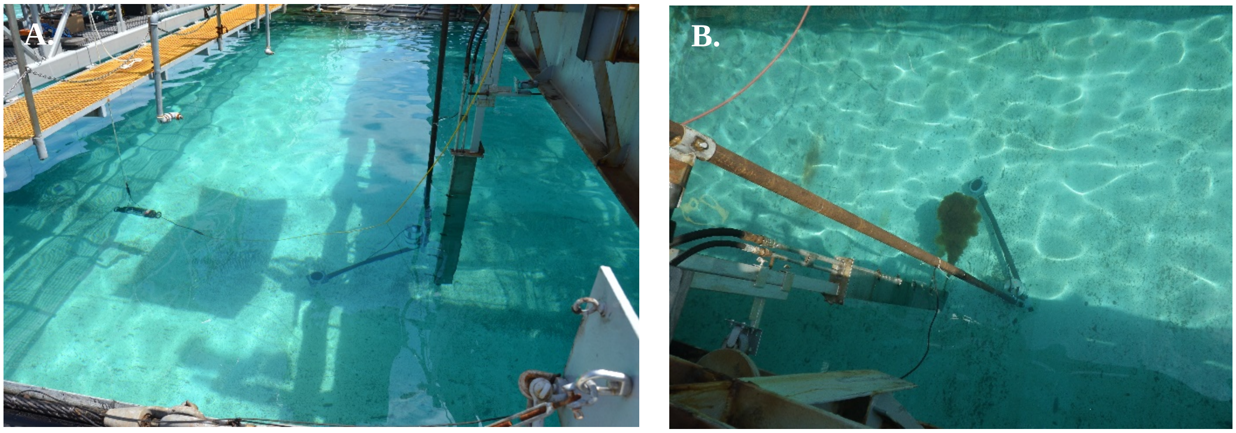

Figure 4. A. Setup for subsurface oil release. Manifold attached to main bridge, oil released from lowest nozzle, directed toward auxiliary bridge. B. Acoustic transducer placed directly beneath oil plume.

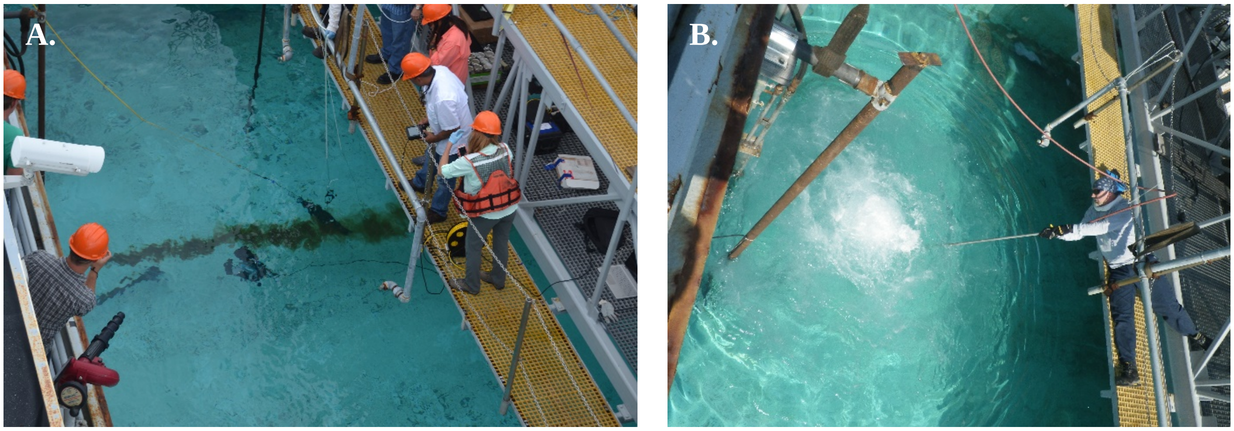

Figure 5. A. Downstream measurements in the oil plume from the auxiliary bridge. B. Subsurface air bubble release over the acoustic transducer.

We measured and evaluated the following LiDAR parameters:

1) backscattering intensity (strength of the return signal from the various oil types, and oil/emulsion thicknesses)
2) Polarization characterization
3) Fluorescence intensity
4) Reflectance

3.1 LIDAR Systems

NRL/SSC owns and operates two above-water LiDAR systems for oceanographic applications A unique characteristic of both these systems is that they are able to modulate the polarization state of the emitted laser light. NRL obtained all required laser-safety approvals prior to the experiment, and followed all laser safety guidelines during deployment. Some of the key differences of both systems are shown in Table 2. The vertical resolution of the LiDAR systems is determined by the laser pulse length and digitizer sampling rate; it is about 11-14 cm (for SLOP) and about 9 cm (for TURBOL). SLOP has been deployed in the field on many occasions and is now a well-polished operational system. TURBOL is a newer system; development started on paper in late 2014 and has only been deployed twice in the field. TURBOL has more capabilities (multispectral emission and detection, higher laser energy) but we decided to also deploy SLOP simultaneously in order to minimize any risk associated with the deployment of a new system. SLOP itself has some advantages over TURBOL, including a better vertical resolution and a faster repetition rate of the laser, so in combination TURBOL and SLOP provided maximum capability and reduced risk.

Table 2. Key differences between SLOP and TURBOL

	SLOP	**TURBOL**
Designed for	Bio-Optical Layer	Turbulence
Laser	Nd-Yag 532 nm	• Nd-Yag 355, 532, 1064 nm • OPO Visible/IR
Polarization	Co and cross linear/circular (fast shot to shot transition)	Polarization rotation/ellipticity possible (slow transition)
Vertical resolution	0.14 m	0.09 m but correlation due to longer laser pulse

3.1.1 SLOP

The Shipboard LiDAR Optical Profiler (SLOP) is a one-of-a-kind science tool used to detect and characterize subsurface layers in the upper ocean while the ship is underway or fixed on a station. One of the unique features is that the LiDAR uses an electro-optical modulator to vary the polarization state of the laser as it exits the system. A set of six detectors with filters measure the different polarization states of light that is scattered out of the water. The combination of range gating and different polarization states are used to differentiate the different particle layers in the ocean. The laser parameters of are shown on Table 3.

Table 3. Laser parameters of the SLOP system

Parameter	**Value**
Wavelength	532 nm
Pulse Width	1 ns FWHM
Pulse Energy	1 mJ
Repetition rate	50 Hz
Beam Size at Aperture	0.6 x 1.23 cm
Beam Divergence	1.79 x 11.7 mrad (measured)

3.1.2 TURBOL

The TURBulence Ocean LiDAR (TURBOL) is an experimental system, aimed at characterizing underwater turbulence by examining the Stokes parameters for elastic and Raman backscattering. The system has been tested successfully in the lab and deployed as a shipborne system in the field in July 2016. In order to reduce risks, a philosophy of simplicity, flexibility and modularity drove the system development. The multispectral and multiple polarization capability in both emission and reception allow the system to be used in the configuration the most relevant to the scientific experiment of interest. Table 4 describes the laser characteristics of TURBOL.

Table 4. Laser parameters of the TURBOL system

Parameter	**Value**
Wavelength	411-703 nm, 532 nm*, 720-2035 nm, 1064 nm*
Pulse Width	8 ns FWHM
Pulse Energy	2.03 mJ, 3.04 mJ, 1.56 mJ, 3.94 mJ
Repetition rate	30 Hz
Beam Size at Aperture (diameter)	1.5 mm, 1.5 mm, 4.0 mm, 4.0 mm
Beam Divergence	15.2 mrad, 23.7 mrad, 7.4 mrad, 29 mrad

*Note values reported for 532 and 1064 specifically, are for the wavelength pump.

3.1.3 LIDAR PROCESSING AND ANALYSIS METHODS

NRL deployed the two LiDAR systems on the moveable auxiliary bridge of the Ohmsett tank facility. After the initial setup and laser firing tests, the first experiment consisted in measuring the backscatter signals from the PVC grid cells. With this setup, the LiDARs can easily be moved lengthwise but are at a fixed distance from the tank sides. As the total the grid cell structure was too large for all individual grid cells to be moved under the LiDARs, most of the individual targets could not be measured individually. As an alternative approach, we did set a specific grid under each LiDAR and added oil progressively to these targets.

Specifically, for SLOP we first measured grid 1, 2 and 8. This correspond to a reference without oil, 1L of ANS and 1L of HOOPS (emulsion). We then set the grid 6 under SLOP and added oil to it in order to set the content to 2L, 3L and 4L (no emulsion).

This first step allows us to calibrate the different lidar channels on clear water and for different oil thicknesses. This experiment allows us to determine a reference which is key to understand the lidar signal. As a second step, we conducted a subsurface oil release experiment under each LiDAR. That allowed us to understand and determine the capability of LiDAR remote sensing to detect and characterized underwater oil plumes.

To understand what the LiDAR measured during this experiment, we have to elaborate on some fundamentals of LiDAR remote sensing. The Lidar equation of the attenuated backscatter return (β) from water molecules, oil and tank bottom (subscript m, oil and bottom, respectively) as a function of depth (z) can be written as:

$$\beta'(z) = \beta_{m,oil,bottom}(z)exp(-2[\tau_m(z) + \tau_{oil}(z)]) \qquad (1)$$

τ_m is the water molecules optical depth, τ_{oil} is the oil optical depth. This equation assumes that the attenuation from non-oils particles in the water can be neglected.

At the bottom of the tank (z_{bottom}), the lidar equation can be written as

$$\beta'(z_{bottom}) = \beta_{bottom}(z_{bottom})exp(-2[\tau_m + \tau_{oil}]) \qquad (2)$$

In absence of oil, this equation reduces to

$$\beta'(z_{bottom}, no\ oil) = \beta_{bottom}(z_{bottom})exp(-2[\tau_m]) \qquad (3)$$

This implies that we can use a reference of signal without oil to determine the optical depth of oil:

$$\tau_{oil} = -\frac{1}{2} log\left(\frac{\beta'(z_{bottom})}{\beta'(z_{bottom}, no\ oil)}\right) \qquad (4)$$

Interestingly, when Eq. 1 is used as a ratio (Eq. 4), the assumption on the absence of attenuation from non-oil particles reduces to an assumption of (statistically) constant attenuation, which is reasonable in a controlled tank experiment.

For Fluorescence, the inelastic scattering can be written using the function F which represents the fluorescence efficiency.

$$F' = Fexp(-2[\tau_m(z) + \tau_{oil}(z)]) \qquad (5)$$

Based on the results from the ROW and LiDAR data, we can see that F is a function of the oil thickness.

3.2 Ancillary Above-Water Measurements

3.2.1 Fluorescence

We used a non-contact, above-water, pulsed ultra-violet (UV) LED sensor to measure oil fluorescence, and subsequently to estimate surface oil thickness of the grid cells. We used the Remote Optical Watcher (ROW) model O-2311A instrument manufactured by Laser Diagnostic Instruments, which pulses a UV beam at the oil surface and measures the oil's stimulated fluorescence. This instrument has an advertised oil thickness detection limit/sensitivity of 1µm, although we observed an even lower detection limit (~ 0.25 µm) during our laboratory calibration experiment.

Although the manufacturer claims the instrument is only designed to detect oil on water, we investigated whether the instrument was also capable of estimating oil thickness, by measuring the fluorescence signal response of known oil thicknesses. Prior to deployment at Ohmsett, the sensor was calibrated in the lab at NRL using HOOPS crude oil provided by BSEE. Measured volumes of oil were added incrementally to a small tank filled with clean, filtered water, to determine the fluorescence response for known oil thicknesses (thickness determined from volume of oil added and surface area of the tank). A calibration curve was determined from these data to enable conversion from measured signal level (in arbitrary units, A.U.) to oil thickness. We observed a linear fluorescence response at low oil concentrations/thicknesses (0 – 7.5 µm) and a non-linear (exponential) response at higher concentrations/thicknesses (7.5 – 60 µm). At oil concentrations/thicknesses over 60 µm (corresponding to a fluorescence signal level of 20,000 A.U.), the signal did not increase with oil thickness, so this technique cannot resolve surface oil thicknesses greater than that. We developed a combined calibration curve encompassing both the linear and exponential ranges, with the break point between the two best-fit equations at a signal level of 10,000 A.U. See Figure 6.

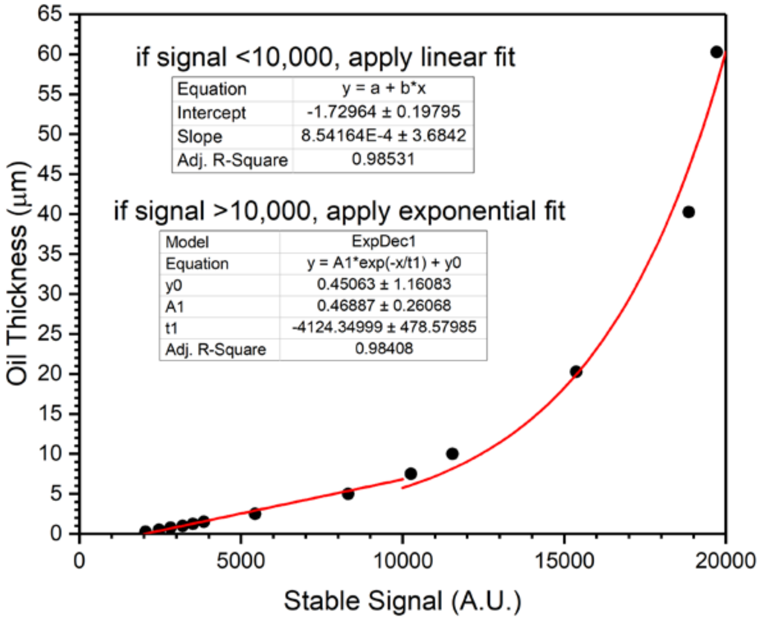

Figure 6. ROW calibration curves (combined linear and exponential responses) based on laboratory measurements. Oil thickness vs. fluorescence signal.

3.2.2 Thermal (FLIR)

A hand-held, forward-looking infra-red (FLIR) spot thermal camera was used to measure surface temperatures of the clear-water and oiled surfaces of the grid cells. The sensor is model TG167 manufactured by FLIR Systems (https://www.flir.com/products/tg167/). The detector is a focal plane array with a 25° x 19.6° field-of-view covering the 8-14 µm spectral range with a resolution of 80 x 60 pixels. Accuracy is ± 1.5% or 1.5° C. Temperature images are stored in a bitmap format. The goal is to assess whether temperature differences between oiled and un-oiled water surfaces (ΔT) can be used to estimate surface oil thicknesses.

3.3 Ancillary In-Water Measurements

3.3.1 Acoustic (AZFP)

The Acoustic Zooplankton Fish Profiler (AZFP) is a calibrated scientific echosounder made by ASL Environmental Sciences. It is an active multi-frequency sonar system that is capable of autonomous operation for up to 12 months at a time. Common deployment methods of the AZFP include subsea moorings (taut line or bottom frame), or more recently via autonomous vehicles such as gliders [R. Chave et al., 2018], illustrated in Figure 7. The AZFP supports as many as four channels, and each channel may operate at a unique center frequency. Because the AZFP is a calibrated sonar system, the intensity of the acoustic backscatter that is received on each channel is known on an absolute scale (i.e. it is compared against an absolute reference level).

The AZFP signal path is shown in Figure 8. The transmit (Tx) pulse is transmitted into the water by the transducer, and acoustical returns are received by the same transducer. Received (Rx) signals are amplified and bandpass filtered, and are then passed through an envelope detector. Lastly, the voltage signal out of the envelope detector is digitized by the analog-to-digital converter (A/D). In the case where a single point target was ensonified, absolute target strength (TS) may be computed instead of A/D counts (N). In the case where a distributed target such as an oil plume was ensonified, the absolute volume backscattering intensity level (Sv) may be computed. The AZFP may directly compute TS or Sv, and it estimates the range to the target(s) by time of flight.

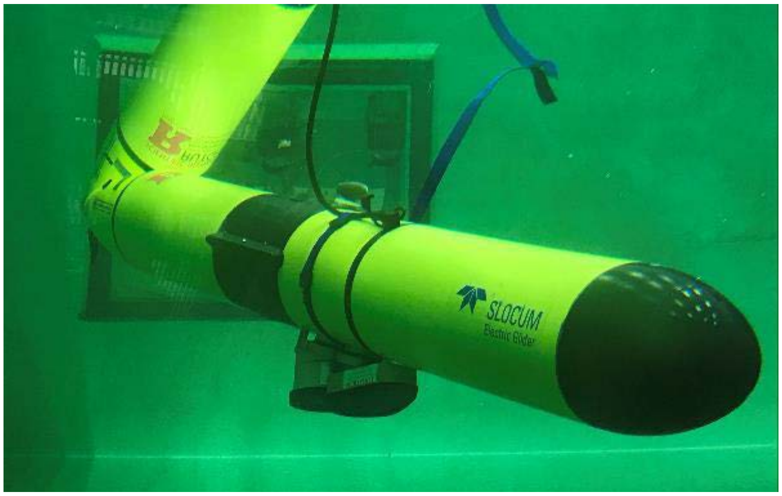

Figure 7. Multifrequency AZFP integrated into Slocum glider (transducer protruding below).

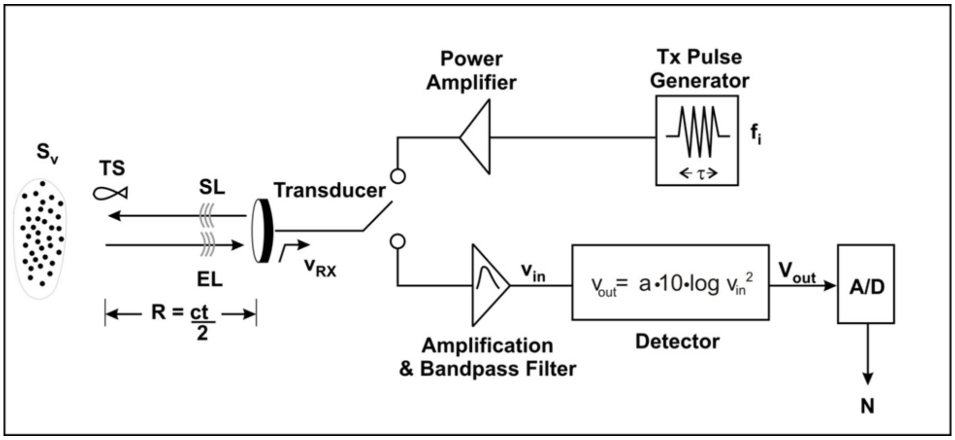

Figure 8. Signal path of the AZFP.

Obtaining the absolute backscatter intensity (either TS or Sv) at each frequency is useful because it facilitates characterization of the target(s) that produced the backscatter. In the context of zooplankton, calibrated backscatter data from the AZFP have been used to differentiate one type of target from another [M. Kitamura et al., 2017], and to estimate the volume and population density of the targets [K. Sawada et al., 2016]. Separately, theoretical models have been developed for the acoustical backscatter from oil in water [H. Medwin, 2005] and have been compared against the acoustical backscatter of gas bubbles in water [P.D. Panetta et al., 2014, report to BSEE]. This research illustrates the benefits of using a calibrated echosounder for target identification and characterization, since the observed (absolute) acoustical backscattering intensity at each frequency may be compared against model predictions.

Processing of the acoustical data collected during the Ohmsett experiment began with computation of the volume backscattering strength, Sv (dB ref. 1 m^{-1}), for each frequency. Acoustical backscatter measurements were converted to volume backscattering strength as follows:

$$S_v = EL_{max} - \frac{2.5}{a} + \frac{N}{26214a} - TVR - 20logV_{TX} + 20logR + 2\alpha R - 10log\left(\frac{c\tau\varphi}{2}\right)$$

where EL_{max} is the echo level (in dB ref. 1 µPa) at the transducer that produces full-scale output from the detector (i.e. when V_{out} = 2.5 Volts). The parameter *a* (in volts/dB) is the slope of the detector response; N, in counts, is the output from the 16-bit A/D; TVR is the transmit voltage response of the transducer (dB ref. 1 µPa/V @ 1 m); V_{TX} is the transmit voltage; α is the acoustical absorption coefficient (dB/m), c is the sound speed (m/s); and τ is the pulse length (s). R is the range (m), and t is the time (s) at which the echo arrives, and ϕ, the equivalent beam angle, is approximated by

$$\varphi = 1.4\pi(1 - cos\theta)$$

where θ is half the full -3dB beam angle of the transducer.

Volume backscattering strength (Sv) is computed and plotted for each AZFP frequency and for each test. Sv was also computed for the ‘clear water test’ where oil was not being injected. Acoustically-estimated Sv values are then compared against Sv values that were calculated from non-acoustical measurements. To obtain the ‘non-acoustical’ Sv values, the LISST instrument’s ppmv output was used in conjunction with a theoretical backscattering cross section model.

To calculate theoretical Sv values, the LISST data for subsurface oil release “Run 2” (July 27th, approximately 1130 UTC to approximately 1245 UTC) were first used to calculate the number of particles per unit volume ($1/m^3$) using:

$$N_v = \frac{ppmv \cdot 10^{12}}{\frac{4}{3}\pi \cdot a^3}$$

where ppmv is the parts per million by volume measured by the LISST for radius bin values from 1.36 µm to 230 µm. The backscattering cross section σ_{bs} (m^2) for a single droplet at each radius was estimated using a fluid sphere model [Anderson, 1950], given by:

$$\sigma_{\mathrm{bs}} = k^4 a^6 \cdot \left(\frac{\rho_w \cdot c_w{}^2}{3 \cdot \rho_{oil} \cdot c_{oil}{}^2} - \frac{1}{3} + \frac{\rho_w - \rho_{oil}}{\rho_w + 2 \cdot \rho_{oil}} \right)^2$$

where ρ_{oil}, ρ_{w}, c_{oil} and c_{w} are the densities and compressional wave speeds in the oil and tank water, respectively (859 kg/m^3, 1019 kg/m^3, 1380 m/s and 1535 m/s). The wavenumber k is computed from $2\pi f/c_w$, where f is the AZFP transducer frequency in Hz (455000, 769000, 1250000 and 2000000 Hz). Once σ_{bs} has been determined, TS may be calculated from the backscatter cross section as $10*\log_{10}(\sigma_{\mathrm{bs}})$.

The linear volume backscatter s_v at each radius value measured by the LISST was computed from σ_{bs} using the number of particles per unit volume N_v:

$$s_v = 10^{\frac{TS}{10}} N_v = \sigma_{bs} N_v$$

and the total volume backscatter over all the LISST radius bins was computed by summing the linear $\underline{s_v}$ values for all radius bins. Linear s_v values were converted to log space via $Sv = 10*\log10(s_v)$, and these (logarithmic) values for Sv were compared against the AZFP-estimated Sv values.

3.3.2 Optical (LISST, fluorescence)

A Laser *In Situ* Scattering and Transmissometry probe (LISST-100X, Type C, Sequoia Scientific, Inc.) was used to measure Droplet Size Distribution (DSD), Mean Diameter (MD) or Volume Mean Diameter (VMD), and Total Volume Concentration (TVC) as per US EPA QAPP L0030110-QP-1-0, SOP 5. The angular scattering distribution from the 32 ring-detectors was processed with manufacturer-provided inversion algorithm that automatically calculates volume concentrations (in µL/L) for 32 logarithmically spaced size bins ranging from 2.50 to 500 µm, along with output of 10 other parameters including laser transmitted power, laser reference power in calibrated units, pressure, temperature, optical transmission, and beam-attenuation. The LISST was deployed in the Ohmsett tank and placed within the oil plume to verify oil droplet size. This *in situ* instrument was also adapted for calibration within the laboratory using a small volume full path mixing chamber mounted to the optics of the LISST-100X. A standard curve of Hoops Crude oil physically dispersed in water was prepared and diluted if the total oil droplet concentration of the solution was larger than the upper limit of detection of the LISST-100X (Figure 9). 100 mL sample was added to the chamber and measurements were collected for 30 to 60 seconds yielding average DSD, MD, and TVC. A linear increase in TVC with increasing oil in water concentrations is presented in Table 5 and Figure 9.

The aforementioned standard curve of Hoops Crude oil dispersed in water was also analyzed for fluorescence intensity via YSI EXO (Xylem, Inc.) and UviLux (Chelsea Technologies Group) fluorometers. Solutions were prepared and placed in a sample chamber large enough to cover the optical probes and/or pressure windows. Fluorescence was measured at wavelengths centered on Excitation / Emission (Ex/Em) of 365/480 nm and 240/360 nm, respectively. Analysis of solutions followed established methods for blank subtraction, and conversion to known standards as outlined in the manufacturer's manuals. Standard curves are shown in Figure 10. Fluorescence intensity of the oil plumes within the Ohmsett tank was gathered via vertically profiling the EXO by rope and deploying the UviLux on a tethered underwater Deep Trekker ROV (remotely operated vehicle) that could maneuver within the plume.

Table 5. Summary of Hoops Crude oil calibration.

Oil in Water	**LISST-TPC**	**EXO-1**	**Uvi-LUX**
ppm	**uL/L**	**fDOM QSU**	**Fluorescence Output**
Bottled water	0.10	0.36	125
Tap water	1	5	484
6	2	12	570
14	5	28	647
28	11	38	735
138	70	174	1946
276	196	332	3864
414	285	275	4170

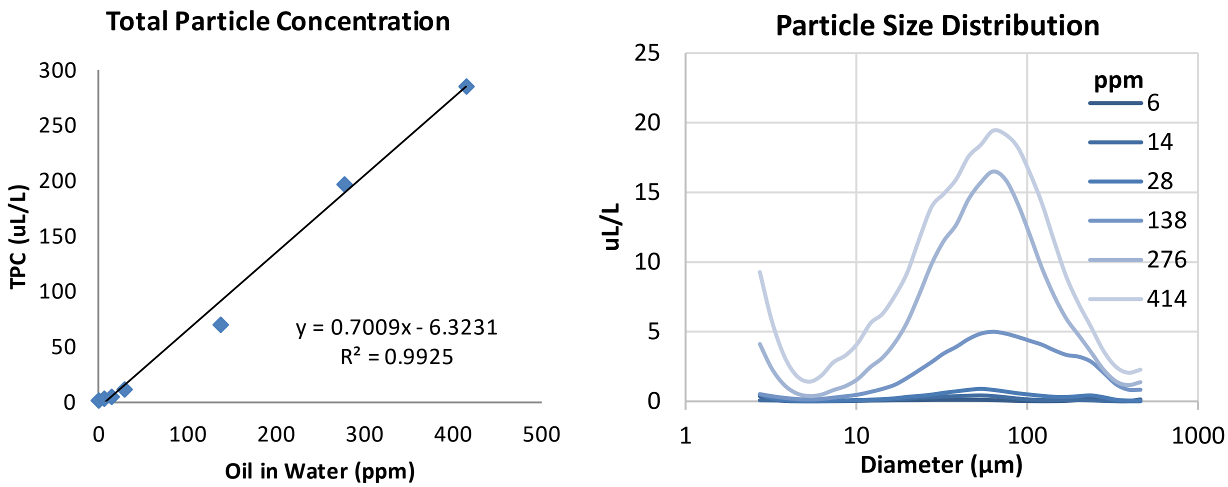

Figure 9. LISST total particle concentration standard curve and droplet size distribution using Hoops Crude oil.

3.3.3 Chemical (hydrocarbon analyses)

Oil plume samples were collected using a niskin water sampler (1 L collection volume) and a ROV fitted with an autosampler (100 mL collection volume). Sample collection was limited to one release on 07-26-18 from 11:30 to 12:15 hours. The characteristics of the plume is expected to be similar for the other releases.

The samples were analyzed for monoaromatic hydrocarbons (i.e., benzene, toluene, ethylbenzene and xylene; BTEX), polycyclic aromatic hydrocarbons (PAHs), alkanes (C10-C35 normal aliphatics, and branched alkanes [pristine and phytane]) and total petroleum hydrocarbons (TPH; as total extracted petroleum hydrocarbons). PAHs analyzed included 2-4 ring compounds and their alkylated homologs (i.e., C0-C4 naphthalenes, C0-C4 phenanthrenes, C0-C3 fluorenes, C0-C4 dibenzothiophenes, C0-C4 napthobenzothiophenes, C0-C4 pyrenes and C0-C4 chrysenes). Concentrations of the detected alkanes and PAHs were summed to compute total alkane and PAH concentrations, respectively. For Alkanes, PAHs and TPH measurements, the water sample was extracted with dichloromethane and concentrated under flowing nitrogen to a final volume of 0.5 mL prior to analysis.

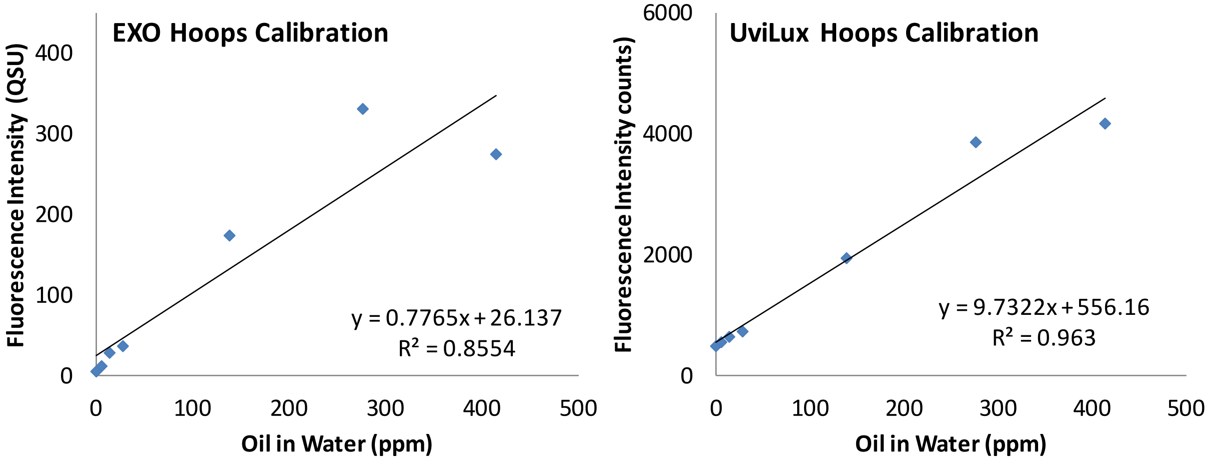

Figure 10. EXO and UviLux fluorescence standard curves using Hoops Crude oil.

BTEX were quantified using an Agilent 7890A Gas Chromatograph (GC) with a 5975C mass selective detector (MSD) with Triple Axis Detector and CombiPal autosampler (CTC Analytics) following EPA Method 524.3 modified to perform head space analysis instead of purge and trap. Alkanes and PAHs were quantified using an Agilent 6890N GC with an Agilent 5975 MSD and an Agilent 7683 series autosampler, equipped with a DB-5 capillary column by J&W Scientific (30 m, 0.25 mm I.D., and 0.25 mm film thickness) and a splitless injection port following EPA NRMRL-LMMD-34-0 SOP. TPHs were quantified with an Agilent 7890B GC equipped with a flame ionization detector (FID) and 7693 autosampler following EPA Method 8015B.

In addition to the oil plume sample collection and analysis, the physical and chemical characteristics of the of the two crudes used in this study are listed below in Table 6, Figure 11 and Figure 12. Alkanes and PAHs were analyzed using the aforementioned GC-MS based method while the density was measured by weighing 1 mL of the crude oil in a closed vial.

Table 6. Physical and Chemical properties of the test oils

	Density at 25°C	**Total Alkanes**	**Total PAHs**	**Hopane**
	g/mL	***ug/mg***		
ANS	0.8763	60.11	21.48	0.08
Hoops	0.8575	62.62	14.74	0.08

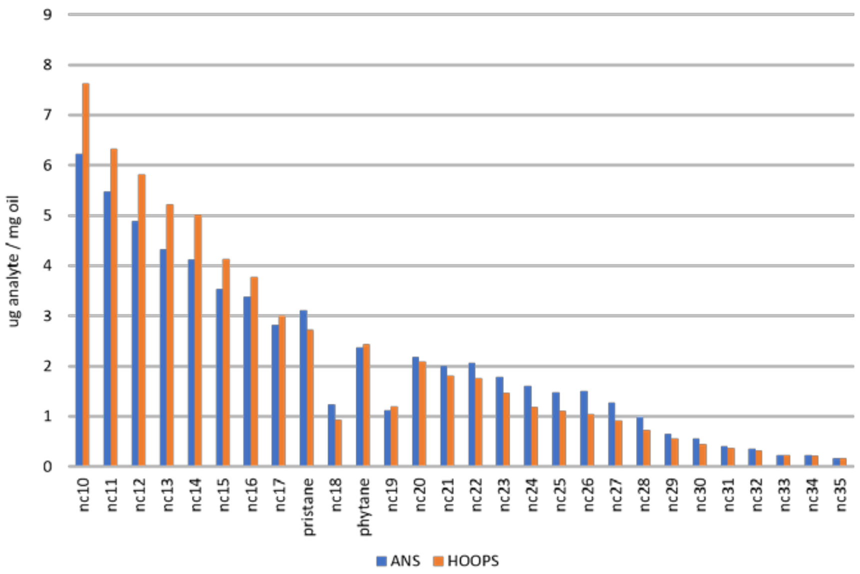

Figure 11. Individual n-alkanes in Alaskan North Slope (ANS) and Hoops crude oil.

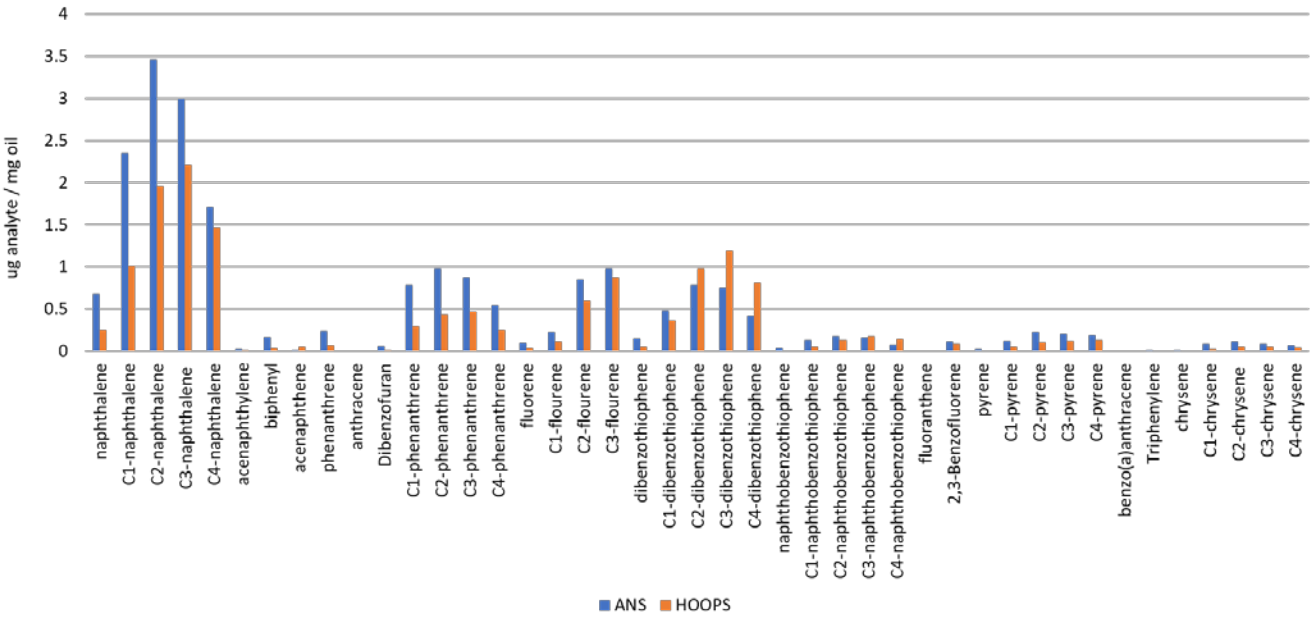

Figure 12. Individual PAHs in Alaskan North Slope (ANS) and Hoops crude oil.

3.4 Aerial and Underwater Imagery

Oscar Garcia (Water Mapping, LLC.) joined us at Ohmsett and participated in the experiment, deploying an unmanned aerial vehicle (UAV) and an underwater remotely operated vehicle (ROV).

3.4.1 Aerial (UAV) Imagery

We utilized the UAV during the surface oil experiment (oil samples of varying types and thicknesses floating in the 3x5 PVC grid cells). The UAV was equipped with three multispectral and thermal camera systems covering ultraviolet to infrared wavelengths (Figure 13A). Imagery collected by these cameras enabled estimation of oil slick thickness. The UAV was suspended from a crane in a fixed position approximately 80' over the grid, such that the field-of-view of the sensors encompassed the entire grid (Figure 13B).

3.4.2 Underwater (ROV) Imagery

The ROV is a DTG2 model from Deeptrekker operated by Water Mapping, LLC. It consists of a small, self-propelled platform equipped with various sensors, a video camera, and a water sampler. The ROV is a tethered system that can measure and transmit real-time fluorometry (hydrocarbon concentration), salinity, temperature, turbidity, and depth. It can also collect water samples and its rated for 450ft water depth. We deployed the ROV during the subsurface oil release to collect underwater video imagery of the plume release, as well as water samples for subsequent laboratory hydrocarbon analyses (Figure 14).

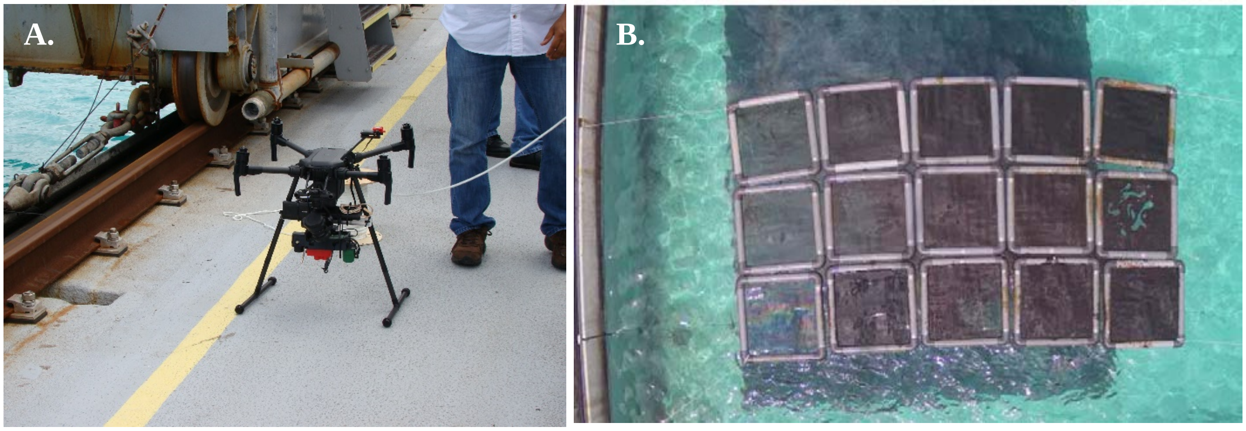

Figure 13. A. UAV equipped with multiple camera systems. B. UAV image of the surface oil-filled grid cells. The grid cell orientation is opposite that shown in Table 1, eg., the clear cell is in the lower left here and the HOOPS crude 5.0 l is in the upper right here. NOTE the 20'x30' dark tarp on the tank bottom below four columns of the grid.

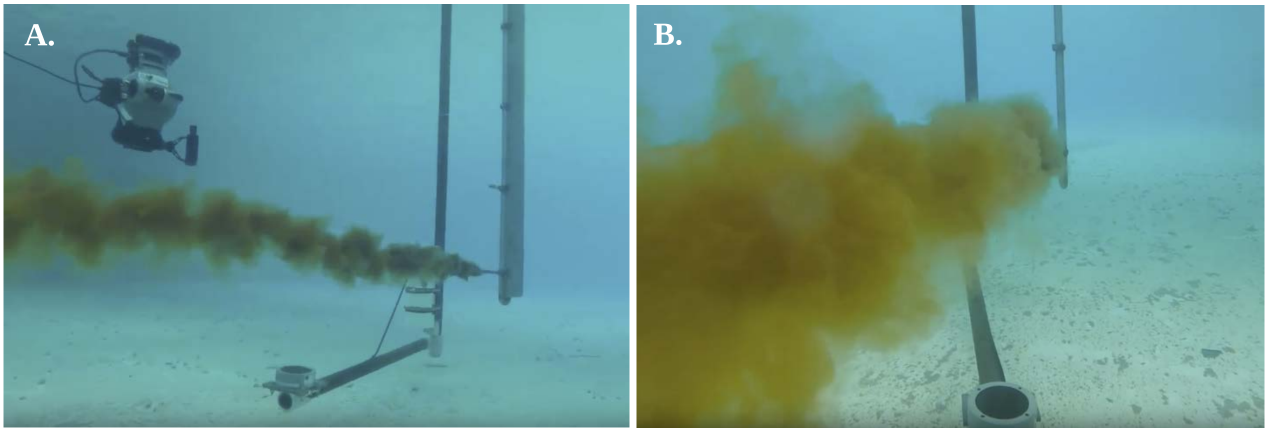

Figure 14. A. ROV operating near the subsurface oil plume in the tank. B. View from the video camera mounted on the ROV. NOTE the acoustic transducer below the plume.

3.5 Event Log

The event log for the week of operations (23-27 July, 2018) is shown below.

Monday, 23 July: Equipment Setup

The day was dedicated to unloading and setting up of the lidar equipment.

- SLOP and Turbol units and their associated cooling systems and deck boxes were set up on the west side of the Auxiliary Bridge, which was located to the north of the Main Bridge.
- Lasers were directed at the water between the two bridges at a height of ~4.2m [Rechecked this with notes in Turbol log taken while targeting beams. 41 in + 57.25 in + 67 in = 165.25 in ~= 13.77ft or ~4.2m] and a pitch of ~19°.
- The control box for Turbol along with the external computers for both lidars were set up in a small shed on the Aux. Bridge to the east of the lidar units.
- While we worked on lidar setup and computer testing, the EPA crew planned a matrix of oils of various surface concentrations to fill a 3 x 5 grid of 1m x 1m squares.
- NOTE: Rick applied grid numbers to matrix during the optics measurements, taken on Tuesday afternoon.

Problems/Issues

- By end of day, SLOPs internal computer was talking to the external computers, however, laser remained disabled. No recorded data.
- Turbol had issues with power and communication with control box.
- The proposed power from the Main Bridge source failed and a large generator was set up on Aux. Bridge.
- A second smaller generator was placed on the Aux. Bridge to handle the computers used with the hand held optics equipment.
- Might have been better to have SLOPs normal 14-15° pitch so that the beam was not hitting the water at that angle. Would this cause a 'loss of signal on return' and is it significant? The angle could not be helped due to the presence of a footbridge below the lidar systems.
- Shed was not really made to protect the external computers and other electronics from the rain and heat. Beginning to wonder if the afternoon heating might be a partial cause of the repeated data acquisition failures, which seemed to occur in the afternoon.

Tuesday, 24 July: Experiment Setup/Initial Measurements

Planned: setup of subsurface equipment for possible Wednesday, rain day; construct the 1m x 1m grid structure for placement of oil; populate the grid structure with varying quantities and types of oils; Rick's hand held optics measurements; lidar measurements.

- Power back to LIDAR at 09:40EDT.
- Tubol awake at 11:30EDT.
- Populated grid at 13:00EDT.
- Rick's measurements of each grid cell (HandHeld, SWIR, FLIR, ROW) at ~14:00-15:00EDT. Grid numbers assigned at this time.
- SLOP turned on at 15:30EDT, no data collected because Ohmsett crew's end of day.

Emulsified Oil Preparation: Emulsions were prepared (45% water content) by mixing 5.4 L of

Ohmsett tank water with 6.6 L of either Hoops or ANS crude oil. A commercial blender was used to prepare 2 L batches at a time. Per batch, 0.9 L water, 1.1 L oil and 2-3 drops of Corexit 9500A was added to the blended and mixed for 2 minutes to prepare the emulsion.

Problems/Issues

- Due to its fixed positions on the Aux. Bridge and the position of the tarp in the tank, we determined that SLOP would be unable to see the two columns of grids toward the eastern side of the tank (the 3 and 5 liter volumes) and Turbol might not see the 5L grids.
- Test firing only, SLOP recorded no data.

TURBOL DATA COLLECTION:

```
24-Jul-2018
              TIME (UTC)
  COMMAND        (HH:MM:SS)
Turbol Start   :  15:31:00
Turbol End      :  15:31:03    0.06 minutes

Turbol Start   :  15:37:20
Turbol End      :  15:37:58    0.64 minutes

Turbol Start   :  15:38:32
Turbol End      :  15:38:42    0.17 minutes

Turbol Start   :  16:38:24
Turbol End      :  16:38:29    0.09 minutes

Turbol Start   :  19:54:35
Turbol End      :  19:56:01    1.43 minutes
```

Wednesday, 25 July: Surface Oil Samples

- Not so much rain as expected, setting up for subsurface release.
- Fire up SLOP to take shots of surface grids: (A) morning, "clear/sheen", "thin film", and "relatively thick"; (B) afternoon, subsurface plume; (C) over large surface collection.

Problems/Issues

- Due to weather (wind and precipitation) overnight, along with expected migration/mingling of oils between squares, the grids today do not contain exactly the same volumes that they were populated with on Tuesday.
- With the position and angle of lidar, along with the size of the target grids (1m x 1m) and the winds and weather, the movement of the floating grid structure made it difficult to center the beams in the target. The targets should have been at least 2m x 2m or more so that SLOP and Turbol could view the same target at the same time. We sampled Grid 1 with SLOP a second time after repositioning the grid structure away from the beam.
- Due to the size of the grid structure and the fixed position of SLOP, there was no way that SLOP could view the largest quantities of oil in Grid cells 4, 5, 9, 10, 14, 15.

SLOP DATA COLLECTION:

```
25-Jul-2018
              TIME (UTC)
  COMMAND       (HH:MM:SS)
Laser Firing     :  18:12:32
Laser Disabled  :  18:17:52     5.33 minutes    OPEN WATER (gains 700,600,600,600)

Laser Firing     :  18:22:54
Laser Disabled  :  18:29:26     6.53 minutes    OPEN WATER (gains 800,700,750,750)

Laser Firing     :  18:36:37
Laser Disabled  :  18:41:40     5.05 minutes    GRID 1 : CLEAR/(lt.sheen), sample 1

Laser Firing     :  18:43:17
Laser Disabled  :  18:47:48     4.52 minutes    GRID 1 : CLEAR/(lt.sheen), sample 2

Laser Firing     :  18:59:10
Laser Disabled  :  19:04:59     5.82 minutes    GRID 2 : ANS crude 1L

Laser Firing     :  19:12:46
Laser Disabled  :  19:17:56     5.17 minutes    GRID 8 : HOOPS emuls. 1L
```

TURBOL DATA COLLECTION:

```
25-Jul-2018
              TIME (UTC)
  COMMAND       (HH:MM:SS)
Turbol Start    :  15:54:38
Turbol End      :  15:55:48    1.17 minutes

Turbol Start    :  15:57:07
Turbol End      :  15:59:52    2.74 minutes

NOTE: ~12:00 EDT, Turbol lost power.

Turbol Start    :  17:40:47
Turbol End      :  17:44:16    3.48 minutes

Turbol Start    :  17:45:52
Turbol End      :  17:46:00    0.14 minutes

Turbol Start    :  17:46:29
Turbol End      :  17:48:03    1.57 minutes
```

Turbol Start : 17:49:28
Turbol End : 17:49:46 0.30 minutes

Turbol Start : 17:49:56
Turbol End : 18:06:30 16.57 minutes

Thursday, 26 July:

(AM) Surface oil samples – LiDARs; pilot plume for acoustics.

(PM) Open-water subsurface oil plume (positioned in line with SLOP).

- Using Grid 6 and Grid 7 (originally HOOPS emuls), the Ohmsett crew added 1.5L HOOPS crude to Grid 7 and 1.9L HOOPS crude to Grid 6. Since the highest volume of oil sampled previously was 1L, we set it up to begin sampling with 2L.
- Rick sampled clear water, no tarp, toward the south side of the tank at ~10:00EDT.
- SLOP turned on at 08:33EDT. SLOP was aimed at Grid 6 and Turbol was aimed at Grid 7.
- Additional HOOPS crude was added sequentially to Grids 6 and 7, to increase measurement volumes to 3L then 4L.
- Rick sampled Grids 6 and 7 (4L samples) after lidar shutdown.
- Set up for pilot plume testing; EPA/Water Mapping data collection (UAV, ROV).

Problems/Issues

Morning:

- Because of the size of the targets (1m x 1m) and the winds causing the grids to move in and out of laser's footprint, there was contamination of the lidar signal at the surface (we zapped the grid structure).

Afternoon:

- We encountered a possible power issue to SLOP after the bridge started to move and then the start of the oil pump to create the plume. This might have caused a (surge in the volts and a cessation of data acquisition, or heating up of SLOP over the course of day after one of two cooling fans burned out).
- At 14:50 EDT, we moved SLOP's power cord from Main Bridge to the big generator on the Aux. Bridge. Immediate SLOP acquisition error when laser was enabled. No recording of data, SLOP was shutdown for the day.

(HOOPS crude added incrementally to Grids 6 and 7 to achieve final volumes noted below)

SLOP DATA COLLECTION:

26-Jul-2018

TIME (UTC)
COMMAND (HH:MM:SS)
Laser Firing : 13:00:49
Laser Disabled : 13:12:55 12.10 minutes GRID 6/7 : HOOPS crude (2 liters)

Laser Firing : 13:28:58
Laser Disabled : 13:36:13 7.25 minutes GRID 6/7 : HOOPS crude (3 liters)

Laser Firing : 13:41:36

Laser Disabled : 13:47:39 6.05 minutes GRID 6/7 : HOOPS crude (4 liters)

Laser Firing : 13:52:08
Laser Disabled : 13:57:43 5.58 minutes OPEN WATER

(subsurface oil plume positioned under SLOP)
Laser Firing : 17:42:00
Laser Disabled : 17:48:34 6.58 minutes OPEN WATER PLUME (moving #1)
Record Stopped! *SLOP data error, SLOP restart/shutdown*

Laser Firing : 18:11:00
Laser Disabled : 18:15:25 4.65 minutes OPEN WATER PLUME (moving #2)
Record Stopped! *SLOP data error, SLOP restart/shutdown*

Laser Firing : 18:34:00 40.425483, -74.067556
Laser Off : 18:36:30 2.75 minutes OPEN WATER PLUME (moving #3)
Record Stopped! *SLOP data error, SLOP restart/shutdown*

TURBOL DATA COLLECTION:

26-Jul-2018

COMMAND	TIME (UTC) (HH:MM:SS)	
Turbol Start	: 13:04:20	
Turbol End	: 13:08:26	4.09 minutes
Turbol Start	: 13:10:18	
Turbol End	: 13:11:17	0.99 minutes
Turbol Start	: 13:12:16	
Turbol End	: 13:15:26	3.16 minutes
Turbol Start	: 13:33:29	
Turbol End	: 13:40:25	6.93 minutes
Turbol Start	: 13:45:35	
Turbol End	: 13:51:47	6.20 minutes
Turbol Start	: 13:56:15	
Turbol End	: 14:01:57	5.71 minutes
Turbol Start	: 17:46:29	
Turbol End	: 17:54:17	7.79 minutes
Turbol Start	: 18:15:12	
Turbol End	: 18:19:18	4.11 minutes

Turbol Start : 18:39:00
Turbol End : 18:41:29 2.49 minutes

Friday, 27 July:

(AM) Open-water subsurface oil plume (positioned in line with TURBOL).

- ROW (above-water fluorescence) mounted under TURBOL, collected data while TURBOL collected data.

(subsurface oil plume positioned under TURBOL)

SLOP DATA COLLECTION:

27-Jul-2018
TIME (UTC)
COMMAND (HH:MM:SS)
Laser Firing : 12:21:55
Laser Disabled : 12:37:30 15.58 minutes OPEN WATER PLUME (moving)
Record Stopped! *SLOP data error, SLOP restart/shutdown*

TURBOL DATA COLLECTION:

27-Jul-2018
TIME (UTC)
COMMAND (HH:MM:SS)
Turbol Start : 12:21:17
Turbol End : 12:41:19 20.03 minutes

Turbol Start : 12:41:21
Turbol End : 12:44:26 3.09 minutes

Additional Notes:

- Bridge move #1 at ~12:17:00 UTC, SLOP laser enabled prior to bridge stopping at ~12:23:00 UTC for plume rise.
  [from Al Guarino: Bridges started at 100ft mark at north end of tank at 9:18 EDT, moved at 0.25 knots for 1 minute 45 seconds, stopping at the 235.2ft mark.]
- Bridge move #2 at ~12:24:00 UTC, stopped at ~12:29:00 for plume rise.
  [from Al Guarino: Bridges started at 235.5ft mark, moved at 0.25 knots for 2 minutes 30 seconds, stopping at 365.4ft mark.]
- Bridge move #3 at ~12:32:00 UTC, SLOP aquisition failed at ~12:46:34.
  [from Al Guarino: Bridges started at 365.4ft mark, moved at 0.25 knots, stopping at 499.6ft mark when SLOP data acquisition failed.]
- SLOP and Turbol shutdown/packup began at 08:59 EDT.

4. RESULTS

4.1 LIDAR Data

4.1.1 SLOP

For the following data analysis, we assumed that the average oil thickness corresponds to the volume of oil divided by the area of the grid. As we will see, the LiDAR data strongly suggest that it is not always the case and that the reference we use is not always accurate. The temporal variation of the LiDAR measurements is the base of our uncertainty determination but it is likely that this procedure could be improved. The Fig. 3 suggests a high degree of spatial heterogeneity of the thickness within the grid for both the ANS and Hoops Crude oil. This will lead to a possible limitation of the accuracy of the reference we used to calibrate the LiDAR data for thickness measurement retrievals. The difficulty to create an accurate reference is due to the stochastic nature of the oil dispersion processes. For this reason a higher statistics of measurements would be key to improve the LiDAR results. For this experiment, we measured 6 different references in a two day time frame. Measuring at least 10-20 references the same day and repeat the measurements once or twice for a total of 2-3 days of calibration measurements would be easy to achieve and likely to improve the calibration accuracy.

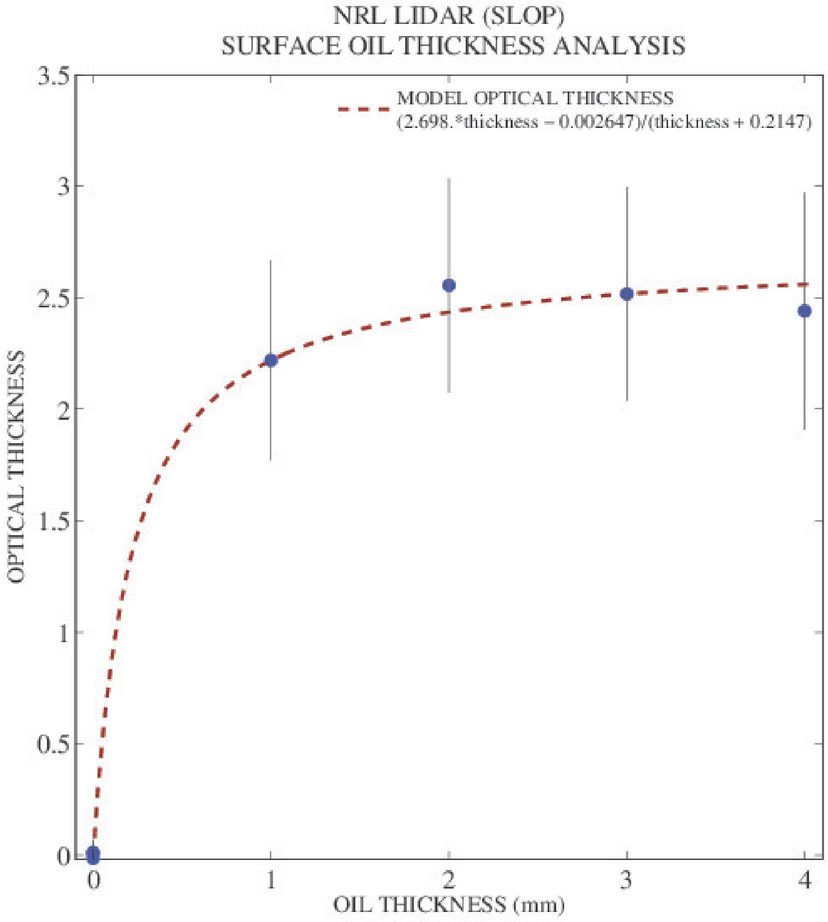

Figure 15. Relationship between oil thickness and oil optical depth (HOOPS only). The vertical line is ± one standard deviation.

Overall, the light of the laser penetrates the layer of oil up to an optical thickness of 2.5. A higher penetration is possible as we didn't make specific tests to determine the highest penetration. It has however to be kept in mind that a typical accepted threshold for LiDAR sensitivity is an optical depth around 3 with variations from system to system. The CALIPSO space LiDAR seems to have a threshold of sensitivity of around 2-2.5 optical depth for daytime and 3-4 for nighttime observations. For Ohmsett experiment, we have demonstrated the lidar penetration in an oil slick equivalent to a 4 mm thickness. Due to the heterogeneity of the spatial distribution of oil but the fact that the LiDAR penetrated reliably the 1mm, 2mm and 3mm oil slick, an accurate statement is that SLOP penetrates an oil slick of 3 mm ±1 mm. For this reason, it is possible to use the attenuation of the bottom of the tank to determine the optical thickness of the oil. It is then straightforward to relate the optical thickness to the oil thickness. Figure 15 shows the attenuation of the bottom of the tank (Eq. 4), as measured by SLOP second receiver (Rx2).

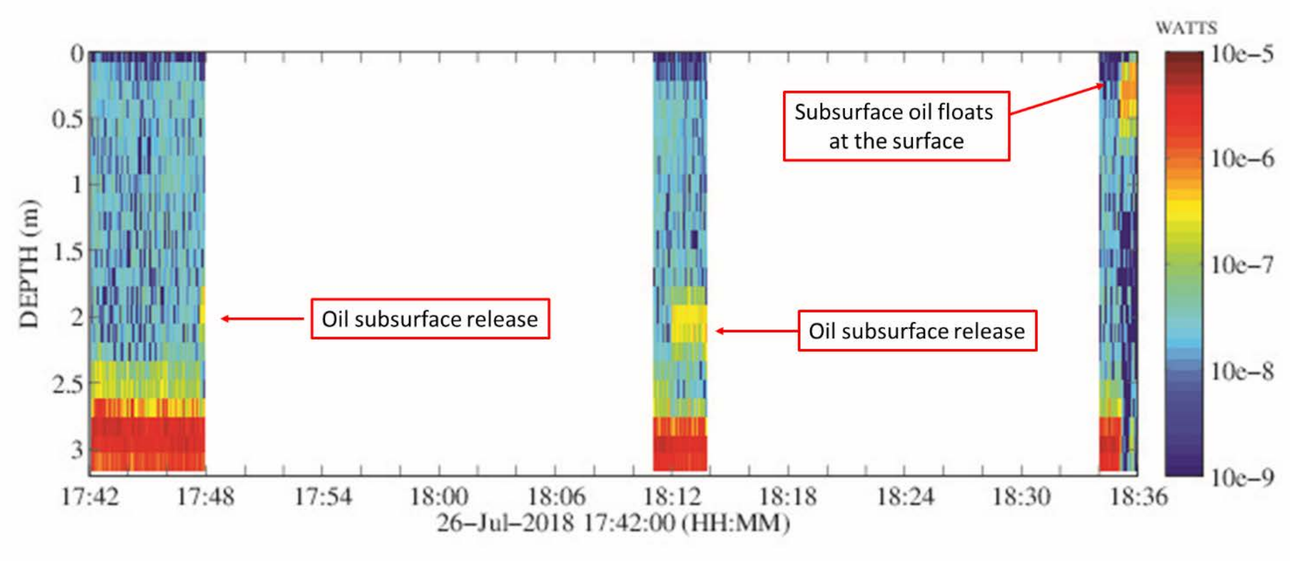

Figure 16. LiDAR profiles as a function of time for the subsurface release experiment.

It is difficult to estimate the exact capability of the LiDAR signal to resolve small differences of oil thickness based on the data shown on Figure 15 and a much larger sample of oil thicknesses with or without emulsions, especially in the 0 to 1 mm range would be required. However, we can still draw interesting conclusions from these data. They suggest that the LiDAR is able to retrieve a very wide range of oil thickness, going from the micrometer to the millimeter scale and with its best resolution power in the 0 to 1 mm range. The loss of linearity of the optical depth to oil thickness relationship between 1 and 3 mm would suggest a lower capability for fine scale resolution in this range. It is possible that the optical thickness measurement shows the equivalent of saturation as the thickness of oil increases and the signal from the bottom is attenuated. Additionally, the data from the thicker oils (both ANS and HOOPS, although only HOOPS data are shown in Figure 15) and the associated uncertainty (vertical line) illustrate the difficulty in getting an accurate reference. It seems likely that the value of the oil thickness we use is wrong for the 4 mm reference. Similarly, the reference provided by ANS (1mm) is not used in Fig. 15 because it was similar to around 100 µm of HOOPS which we believe is more related to the difficulty to obtain a homogeneous layer with ANS than oil characteristics. As we previously mentioned, this statement is suggested by what we can see of the oil heterogeneity (Fig. 3) and will be confirmed by the LiDAR fluorescence measurement.

From the relationship between oil optical depth and oil thickness, we can determine an estimate of the thickness of oil as a function of time during the oil release experiment. The data for the subsurface release with the nozzle set under SLOP are shown on Figure 16 - 18. The LiDAR shutdown unexpectedly several time during the experiment. We suspect an incompatibility with the noise of the power line as the shutdown was triggered by the movement of the bridge. This was an unexpected issue and we didn't bring with us the independent power supply we sometime use on a ship.

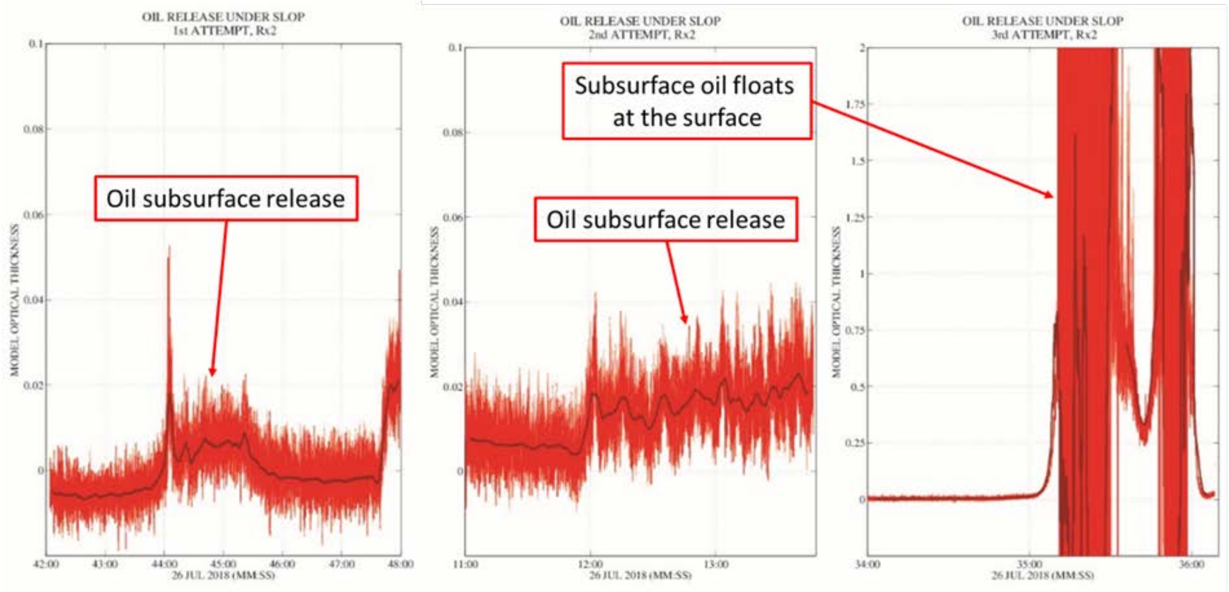

Figure 17. Measurement of oil optical depth as a function of time for the subsurface release experiment.

The limited dataset shown on Fig. 16 still illustrates well the power of LiDAR remote sensing to detect oil underwater. As we can see on Fig. 16, the vertical structure of the oil plume is immediately captured by the LiDAR as it is released. The blue/green area is the water, the yellow/orange feature is the oil released above the bottom of the tank (red feature). Neither SLOP nor TURBOL have an automatic feature classification algorithm and we created a preliminary algorithm for TURBOL that we will show and discuss in a following section. The oil structure can be seen underwater (left and middle segment of Fig. 16) and the top of the oil is at a depth of around 1.7 m. The bottom seems to be 30 to 50 cm above the bottom of the tank. There is some level of uncertainty associated with the bottom altitude determination of an optically thick feature from a nadir looking LiDAR. If the layer fully attenuates the signal, the apparent bottom will be higher than it is in reality as the light will be fully attenuated before reaching the bottom. Therefore, the accuracy of the bottom altitude determination of the oil layer is an open question that we are not yet able to fully address. That being said, as the LiDAR is able to detect the bottom of the tank during the underwater oil release, it means that the light is not fully attenuated and both the determination of the top and bottom we would make using the data shown on Fig. 16 could be accurate.

As we can see the LiDAR can follow the vertical movement of the oil plume and when the bridge stops, we can see the quick rise of the oil plume towards the surface (right segment of Fig. 16). As the oil slick becomes thicker, we can see that the LiDAR is losing sensitivity to the surface at some point (the bottom red feature becomes blue) where the oil thickness is estimated to be over 2.5 mm (Fig. 18).

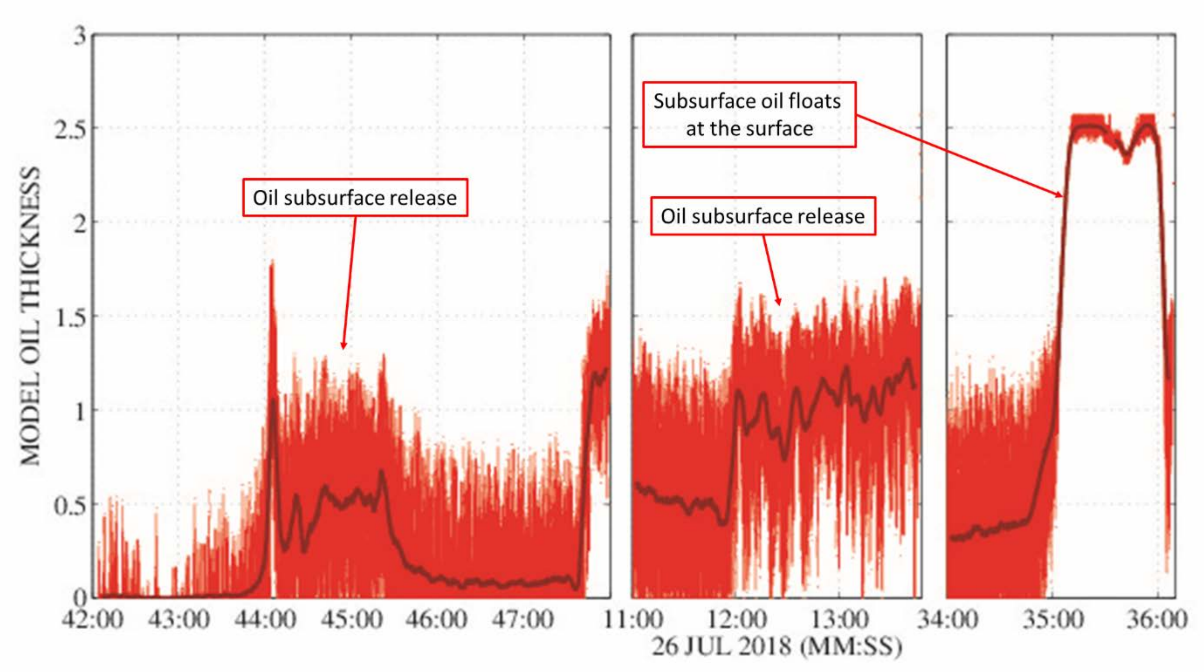

Figure 18. Oil thickness as measured by SLOP during the underwater release (nozzle under SLOP). It's possible that the relationship saturates at 2.5 mm and that there's much more oil in the right panel than we determine here.

Because of this power issue, we setup the nozzle under TURBOL the following day and SLOP was able to record two events of the oil layer spreading at the surface. The data are shown on Figures 19 – 21. There is a clear detection of the oil (yellow structures at altitude 0 m in Fig. 19) and we can see that the bottom of the tank stays visible in the LiDAR observations which is consistent with an oil thickness estimate below 1.25 mm. Note that when the thickness of oil is in the millimeter range, the oil thickness has to be determined from the backscatter intensity (Fig. 15) or fluorescence (see Fig. 23 and associated discussion in the next section) and we cannot use the straight observation of the underwater structure (Fig. 16 and 19) as the minimum thickness it can resolve is limited to the centimeter level (Table 2).

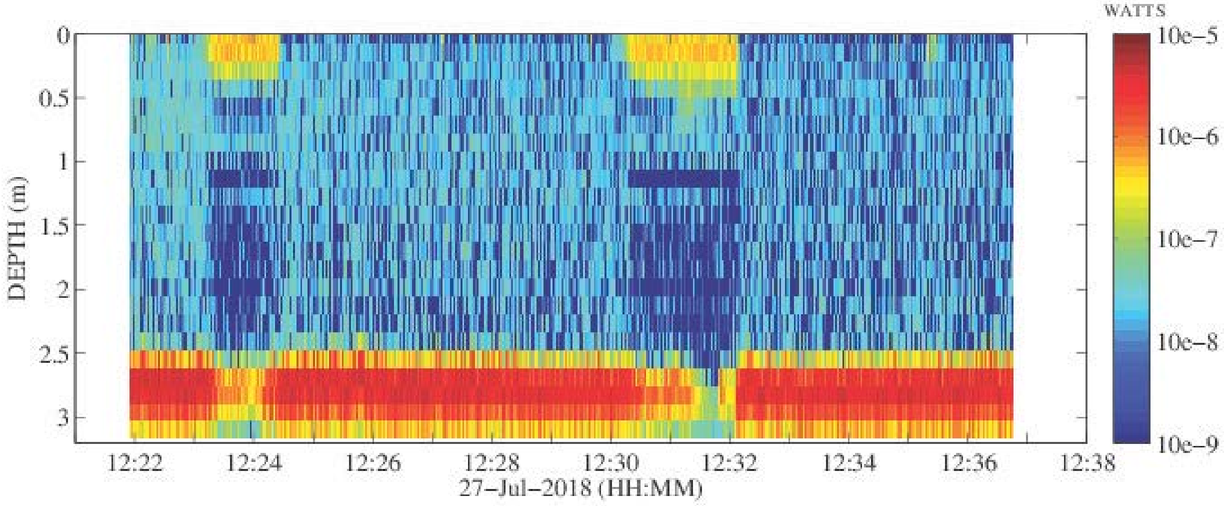

Figure 19. SLOP profiles as a function of time for the subsurface release experiment (nozzle set under TURBOL).

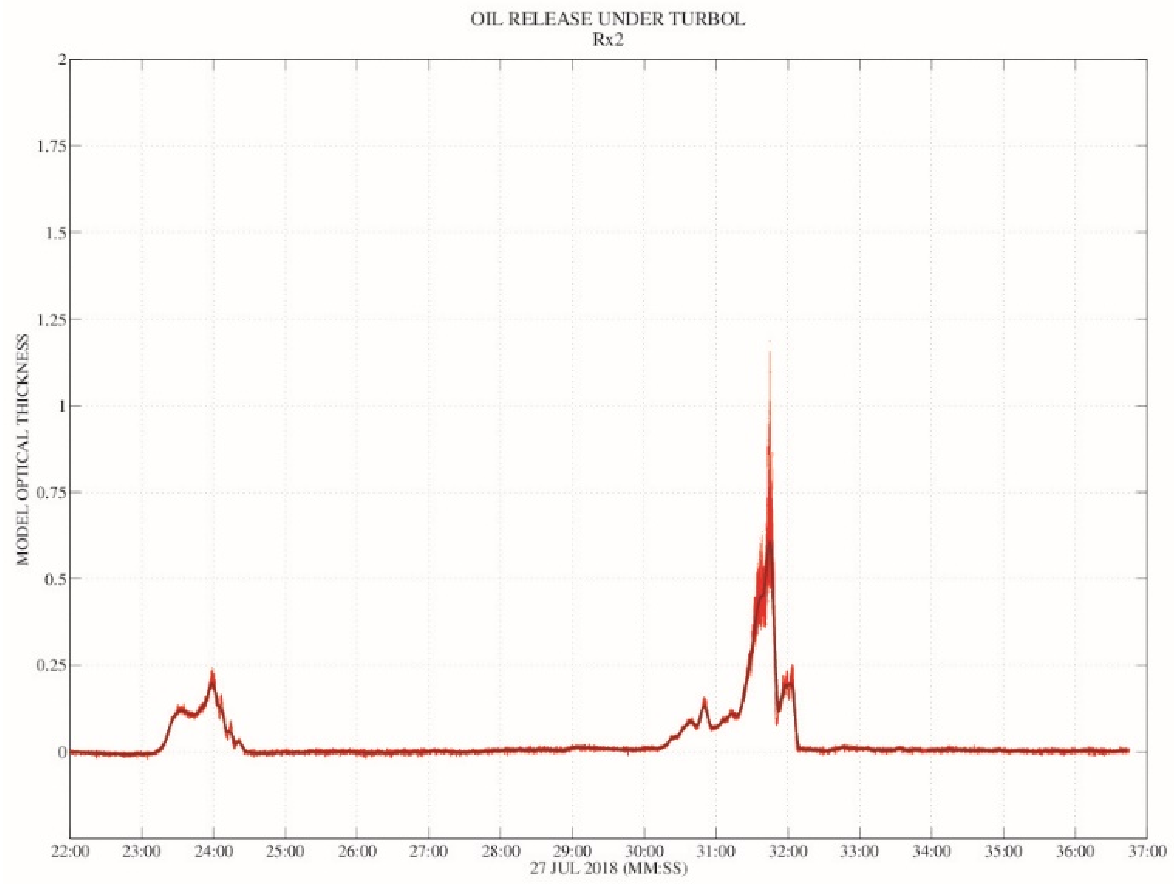

Figure 20. Relationship between oil thickness and oil optical depth as a function of time for SLOP, for the subsurface release experiment (nozzle set under TURBOL).

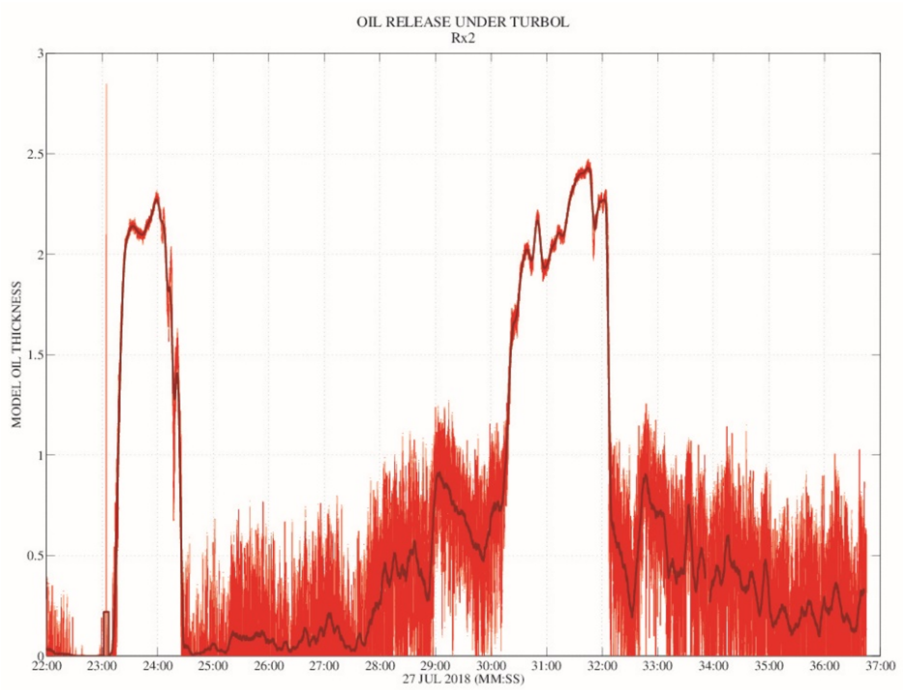

Figure 21. Oil thickness as measured by SLOP during the underwater release (nozzle set under TURBOL).

As a final note on elastic scattering, the retrieval of Fig. 21 does not show a very clear sign of saturation of the oil thickness retrieval in the 2-2.5 mm range. The determination of the maximum penetration of the LiDAR in oil slicks would be a key information to determine the LiDAR retrieval limitations. It would be an interesting objective for a future work.

We will summarize these findings and provide more elements related to the capability and limitations of LiDAR for oil spill detection and thickness measurements in the discussion part of this document.

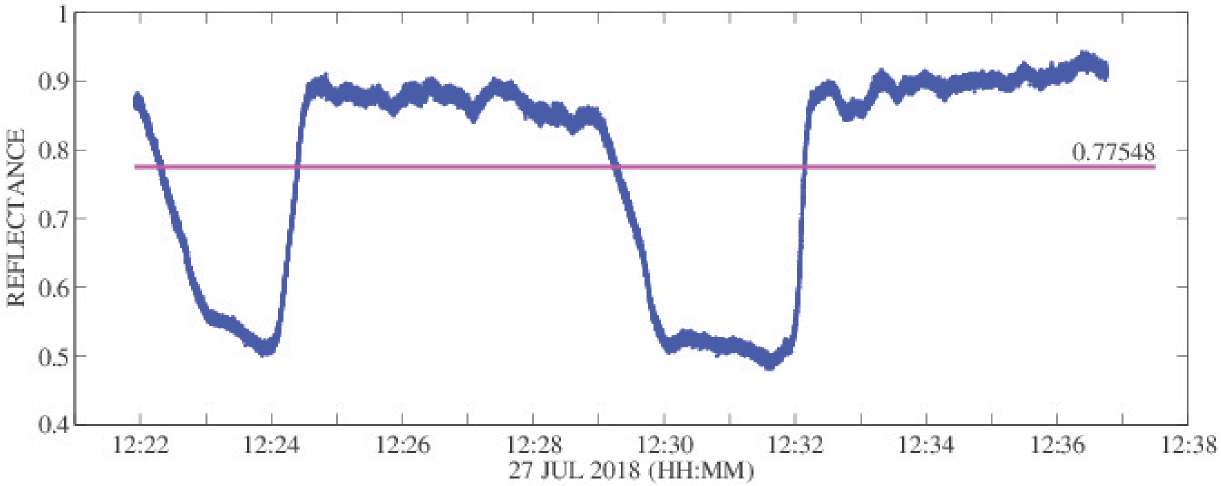

Figure 22. SLOP reflectance at 575 nm (fluorescence channel) as a function of time for the subsurface release experiment (nozzle set under TURBOL). Time axis corresponds to Figure 19.

A note on using the LiDAR as a radiometer: When the laser pulse is not present, the lidar functions as a radiometer and can subsequently measure reflectance (integrated for the surface and subsurface water column). The information is present on each lidar profile and is typically not calibrated or used because the profile information is usually a higher priority. We are showing here the reflectance at 575 nm (fluorescence channel) because it contains an unambiguous signature (Figure 22). The reflectance measurement here would imply that oil at the surface decreases the reflectance. If we look at the release of oil under SLOP (not shown), it seems that the matter is more complex and that oil can sometime increase the reflectance. It is difficult to reach strong conclusions because this channel is not calibrated and we do not measure the sun reflectance, but it does indicate the potential to provide additional useful information related to oil in or on the water, although additional research is needed.

Fluorescence measurement: One of the detector of SLOP was setup with a bandpass filter centered at 575 nm and relatively wide (50 nm) in order to detect Fluorescence**.** As both elastic an inelastic (fluorescence) scattering were measured at the same time, we are able to calibrate the fluorescence intensity in the different grids to determine the relationship between fluorescence and oil thickness. The data are shown on Figure 23. Overall, we can see how the increase of oil thickness relates to an increase of fluorescence intensity.

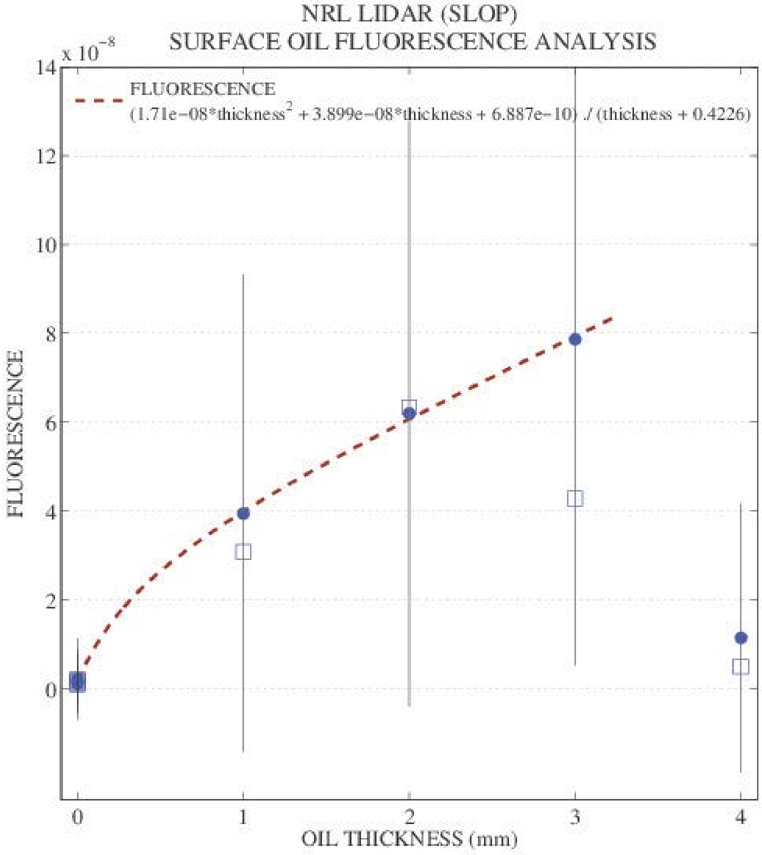

Figure 23. Relationship between SLOP fluorescence data and oil thickness.

As for elastic scattering, it seems that there is an issue with the 4L HOOPS grid and the low value of fluorescence is consistent with a mixing issue and an oil thickness lower than expected.

A key point is that although the fluorescence data of the ROW seem to saturate at larger oil thicknesses, this does not seem to be the case for the fluorescence return of the lidar. A possible explanation could be related to the average power of SLOP laser pulse which is around a megawatt. This is several order of magnitudes above the ROW power budget (< 2W). Additionally, the photomultiplier tubes are very sensitive detectors.

We also investigated the SLOP depolarization ratio as a tool to characterize the oil. Figure 24 shows the depolarization ratio for the oil in the grids. Surface peak is the signal in the oil and bottom peak is the signal at the bottom of the tank (impact of oil on laser forward scattering). It is difficult to reach a strong conclusion. Qualitatively, there is some increase of polarization but it does not seem to be a monotonic relationship. The straightforward oil signature in polarization (Sun et al. 2011) do not seem to apply, and the lack of reference make it difficult to understand if the discrepancy is linked to the type of oil used, a difference of scattering angles or intrinsic differences between passive and active measurements. Additional research is needed.

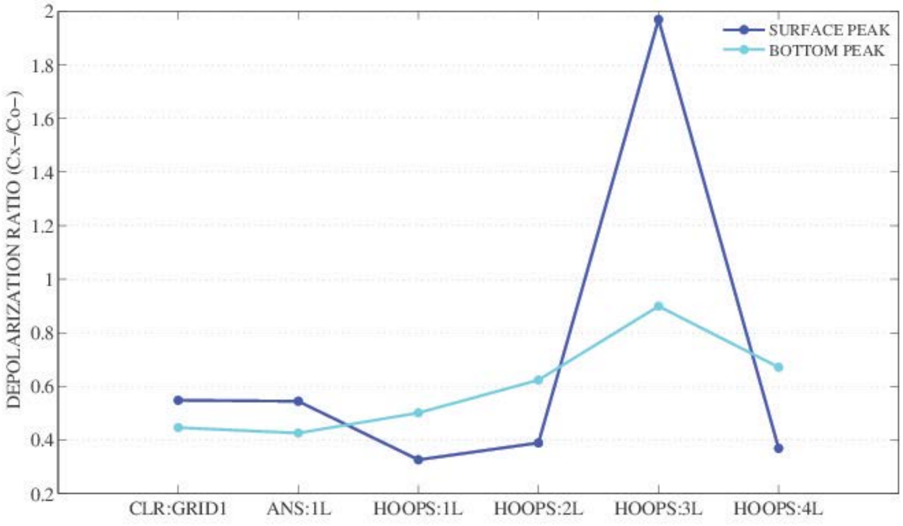

Figure 24. Depolarization ratio for the oil in the grids.

<u>4.1.2 TURBOL</u>

Because the fluorescence channel of SLOP signal to noise ratio was low, it was not apparent from the Graphic User Interface that it was a functional channel. For this reason and because fluorescence was part of the project objective, TURBOL was switched to fluorescence mode for most of the experiment.

TURBOL measured the grid oil thicknesses but the fluorescence channel is more difficult to calibrate than elastic scattering because only the target that fluoresces is a real observation, everything else in the profile is noise. For this reason, calibration of fluorescence requires an internal calibration of the LiDAR (with internal references) which is more difficult to achieve. The main component of the internal reference for TURBOL is the power meter that measures the energy of each shot but it seems that the power of the laser was at times too low to reach the threshold of detection. It is easy to fix by moving the power meter somewhere in the LiDAR where there is less attenuation but the laser issue is new and there wasn't enough energy loss to show an obvious issue with the fluorescence data during the experiment so the power meter malfunction was not discovered before the data analysis. For this reason and the low number of calibration targets we sampled, we are not able to provide a quantification of the fluorescence as a function of oil thickness with TURBOL, as we did for SLOP.

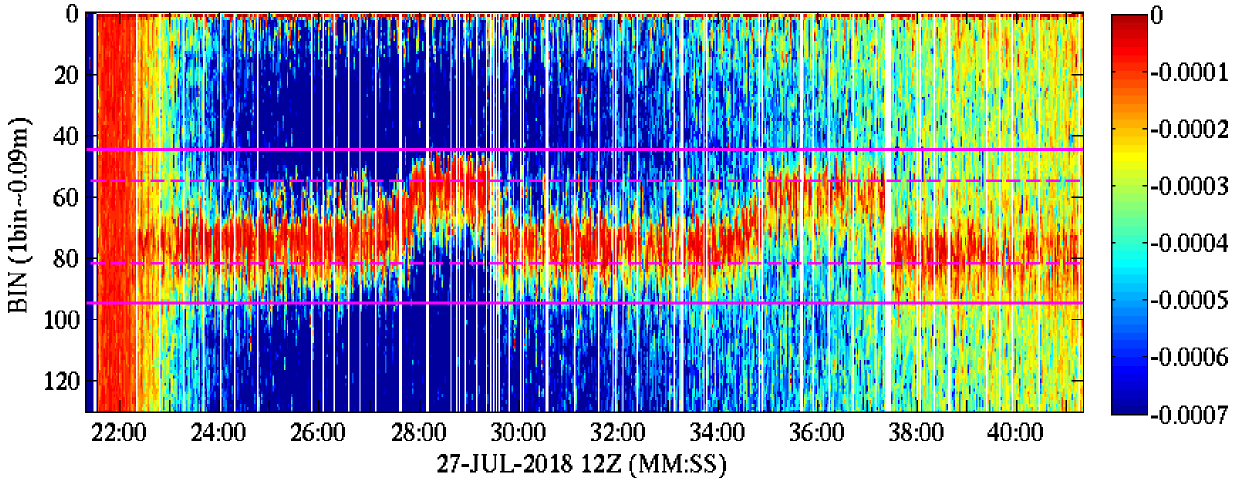

Figure 25. TURBOL fluorescence profiles as a function of time for the subsurface release experiment (nozzle set under TURBOL).

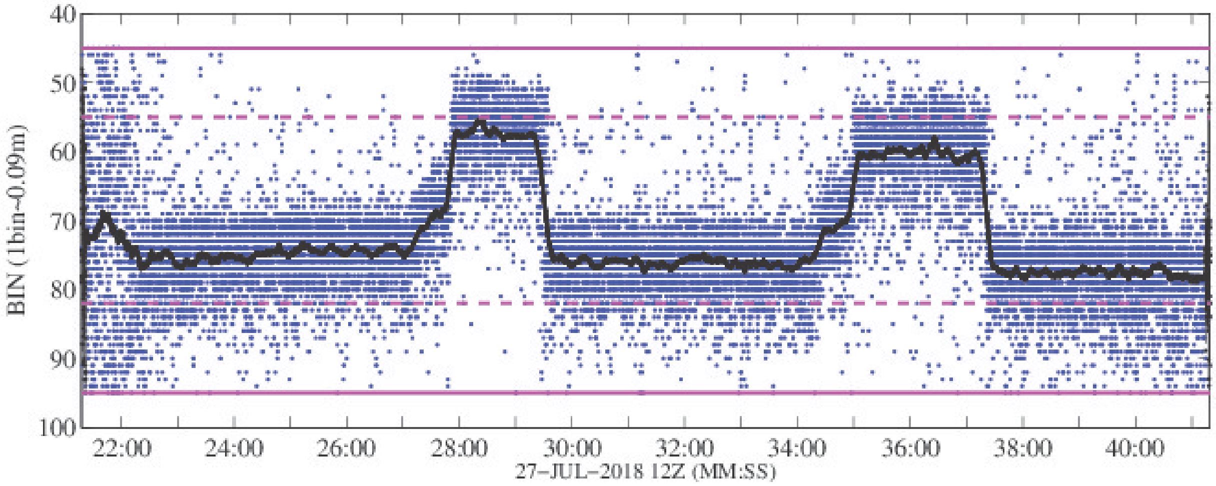

Figure 26. Same as Figure 25 with a highlight of the peak of the signal which is the approximate position of the top of the oil layer.

However, even if we cannot calibrate the fluorescence/oil thickness for TURBOL, the strength of the LiDAR is that it always provide a direct measurement of the vertical structure of everything in the laser path. As we can see on Figures 25 and 26, the LiDAR can perfectly follow the change of depth of the subsurface oil plume. During this experiment, the nozzle was set to release oil directly under TURBOL. The horizontal dotted pink lines represent the top of the water and bottom of the tank. The solid pink lines delimit the domain where the algorithm looked for the top of the oil plume. We started the acquisition of the data as the bridge was moving and TURBOL sees the top of the oil around 2 meter underwater. Each time the bridges stop (around 28:00 and 35:00 on Figures 25 and 26), the oil floats at the surface and we can see that TURBOL measure the variation of depth of the top of the oil as it reaches the surface. Similarly, when the bridges resume their movement (around 29:30 and 37:30), TURBOL can measure the abrupt change of oil depth.

The limitation we previously mentioned for bottom altitude determination with LiDAR still apply. However, based on the data shown on Fig. 25, it is possible that TURBOL penetrates the oil and provides a direct estimate of the oil bottom position. It is however difficult to know for sure because of the novelty of the measurement and the lack of external reference. An underwater camera synchronized with the lidar would be interesting to use to see if the apparent level of penetration of the fluorescence channel in oil correspond to thinner patches. Alternatively, we could design the experiment so that the lidar continues to look at oil as it disperses at the surface (i.e. stop the subsurface release for a few minutes).

4.2 Ancillary Above-Water Measurements

We collected above-water optical measurements including fluorescence from the ROW pulsed LED instrument and thermal signatures from the hand-held FLIR sensor.

4.2.1 Fluorescence

Using the ROW, we collected fluorescence measurements of the variable oil thicknesses in each of the grid cells, and used these data to develop a calibration curve for HOOPS oil during the Ohmsett experiment (Figure 27), similar to the lab approach shown in Figure 6.

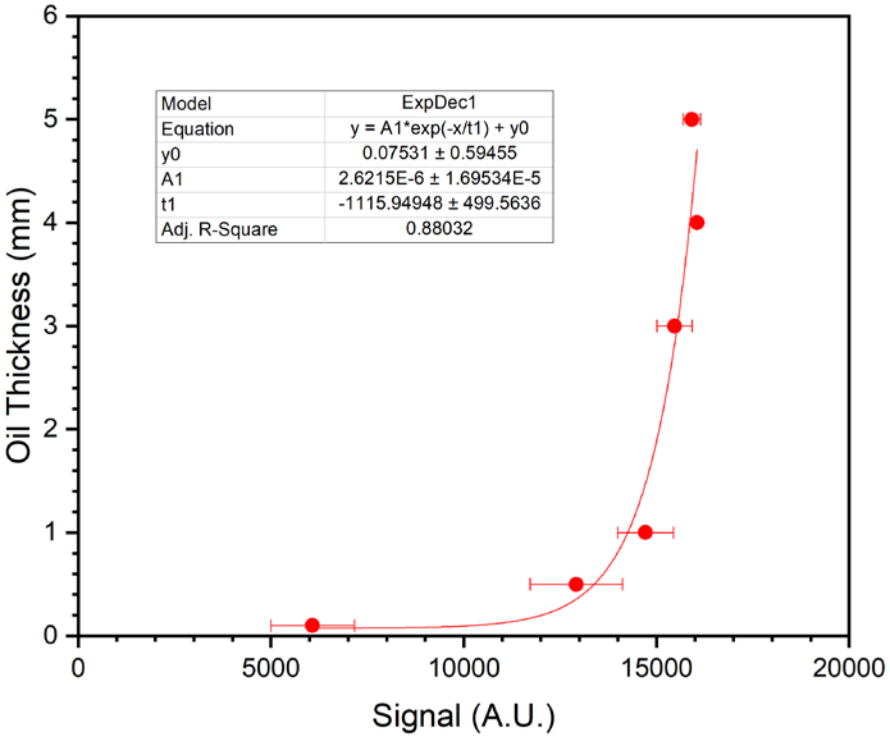

Figure 27. ROW calibration curve based on Ohmsett grid cell measurements. Oil thickness vs. fluorescence signal.

Fluorescence data were collected for each grid cell for approximately 1 minute, enabling us to get an average value as well as a standard deviation (an indicator of within-grid variability). The lab data were collected over a wide range of well-resolved oil thicknesses under indoor (artificial) lighting conditions. The grid cell measurements were collected for only a few widely-spaced oil thicknesses (i.e., poorly-resolved) under natural solar illumination conditions. The different illumination conditions resulted in very different calibration curves. For both the lab and Ohmsett grid calibrations, the fluorescence signals saturated, and thus are not valid to retrieve oil thicknesses above about 20,000 A.U. for the lab calibration (corresponding to an oil thickness of 60 μm) and above about 15,000 A.U. for the Ohmsett grid cell calibration (corresponding to an oil thickness of about 1mm). Also, keep in mind, the grid cell thicknesses were probably not correct, as mentioned before, due to the uneven oil dispersal in the grid cells.

For the subsurface oil release on 27 July, the ROW was mounted to the guard rail on the auxiliary bridge, looking perpendicularly at the water surface directly beneath TURBOL. Autonomous fluorescence measurements were collected while the TURBOL laser fired. Figure 28 shows the ROW fluorescence response as the subsurface oil reached the surface. Figure 29 shows the calculated oil thicknesses, based on both the laboratory and Ohmsett grid cell calibration data. In Figure 29B, thicknesses over 1 mm are not valid, due to signal saturation.

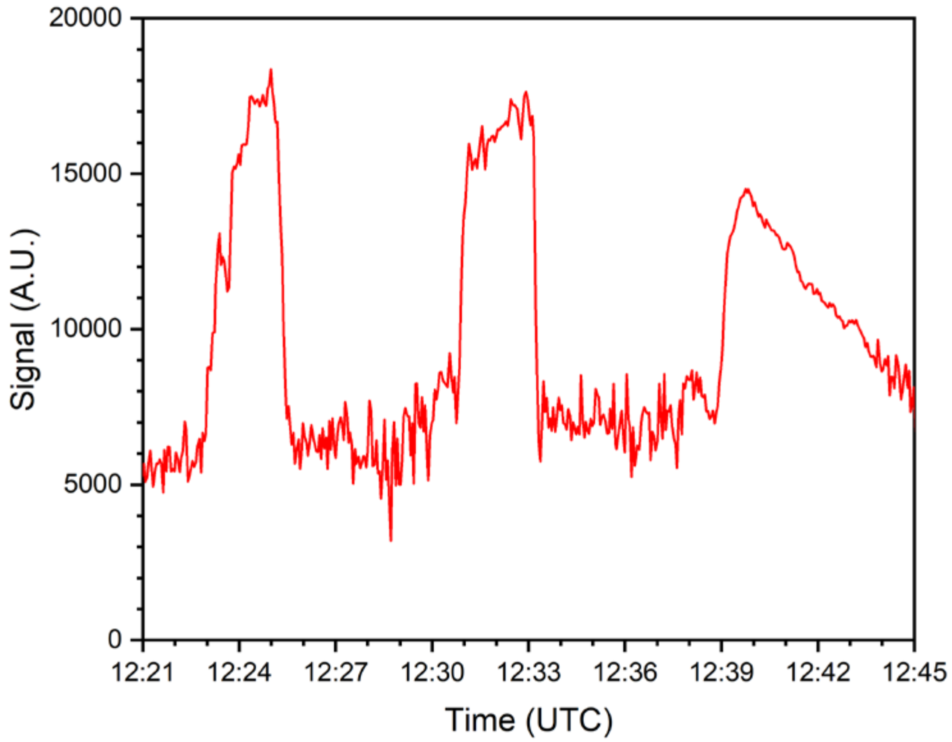

Figure 28. ROW fluorescence signal vs. time, during TURBOL firing on 27 July. The peaks represent the subsurface oil reaching the surface.

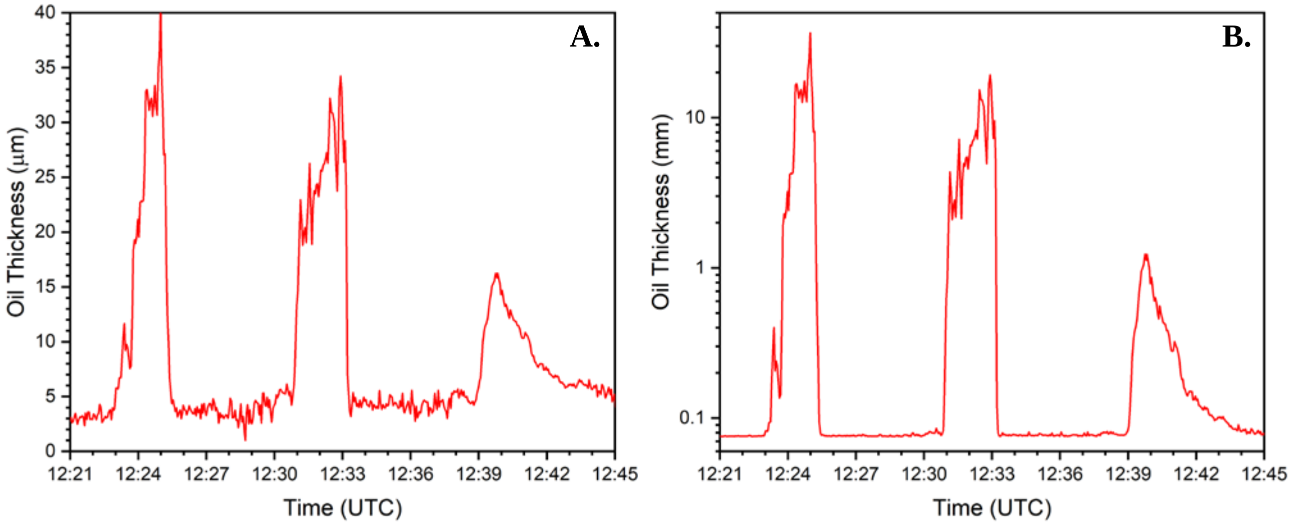

Figure 29. Oil thickness vs. time, during TURBOL firing on 27 July (from ROW fluorescence data in Figure 28). A. Based on laboratory calibration. B. Based on grid cell calibration.

4.2.2 Thermal (FLIR)

We collected surface temperature measurements of the grid cells using the FLIR hand-held thermal camera. The measurements included clear water (no oil), HOOPS crude and emulsified cells, and ANS crude and emulsified cells. We then calculated the temperature difference between the clear water and oiled water samples (ΔT) and developed empirical, best-fit regression equations to estimate oil thickness from ΔT. Because the thermal differences for the crude and emulsified samples were likely different (due to the inclusion of water in the emulsified samples), we developed separate curves for each (Figure 30). However, because grid cells 11-15 containing the variable HOOPS crude concentrations were not measured with the FLIR, only 3 data points are available for the crude oil thickness estimation.

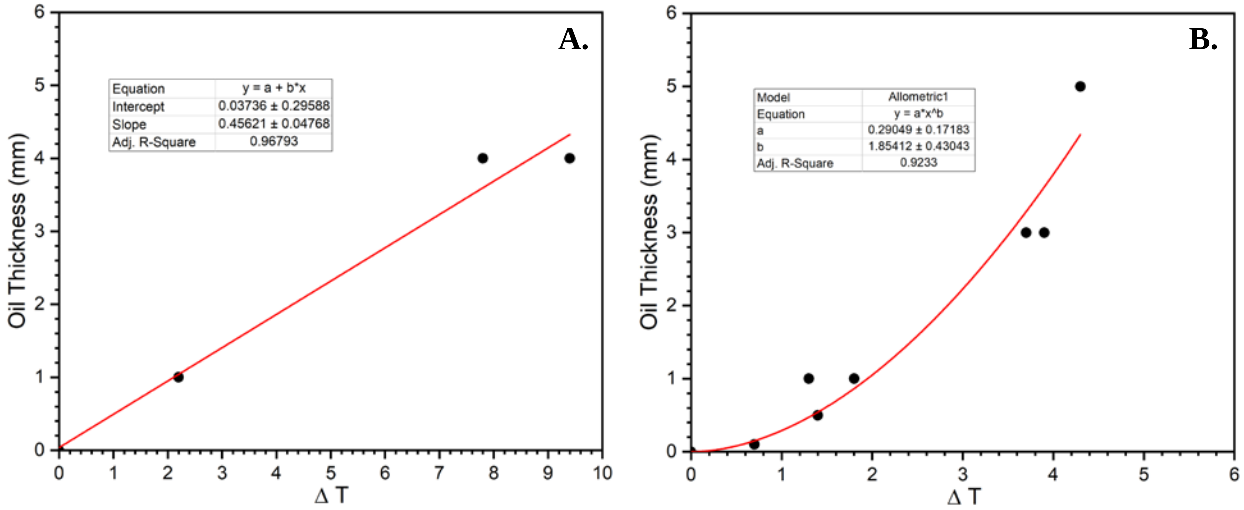

Figure 30. Oil thickness vs. ΔT. A. Crude oil (ANS and HOOPS combined). B. Emulsified oil (ANS and HOOPS combined).

Also, measurements for the ANS and HOOPS oils are combined, for both the crude and emulsified samples. In other words, there are not separate relationships for each oil type; that would be interesting, but would require measurements for additional oil concentrations for both crude and emulsified samples, for both oil types.

4.3 Ancillary In-Water Measurements

4.3.1 Acoustic (AZFP)

The upward-looking AZFP collected data during a ‘clear water’ test where no oil was being injected and the bridge was stationary (July 23rd), during multiple trials where the bridge was moving and oil was being injected (July 26th and 27th), and also when air was being injected alongside HOOPS oil (July 27th). Each figure lists data acquisition times in UTC. For each figure, the vertical axis is range (m) from the instrument, and the horizontal axis is time. Bright colors correspond to stronger returns per the colormap legend.

Figure 31 presents results obtained when the AZFP was looking at clear water. The purpose of the test was to transmit with different pulse lengths, to assess the impact of pulse length on the data from each channel, and to inform pulse length selection in future tests. Five different configurations were attempted. In the first trial, the pulse length at each frequency was 1000 us, and in the second trial the pulse length was lowered to 700 us. In the third and fourth trials, pulse length for each frequency was 400 us and 150 us, respectively. In the fifth and final test, pulse length was 150 us for the 455 kHz and 769 kHz channels, 100 us for the 1250 kHz channel, and 85 us for the 2000 kHz channel.

Figure 32 plots the data from the first release of crude HOOPS oil on July 26th. Initially, the platform was stationary and a slight amount of oil was released (annotation #1). Next (annotation #2), the oil flow was increased and the bridge began moving. Later (annotation #3) the AZFP mounting pole was pivoted, and then the platform ceased moving (annotation #4).

The data plotted in Figure 33 show the results from a series of tests later on July 26th. During this trial, the AZFP began recording prior to oil release. When the platform began moving (annotation #1) while oil was released, the plume was visible. As the platform stopped the first time (annotation #2) the plume was seen to rise. Platform motion and oil release were resumed (annotation #3), and then stopped (annotation #4). After the bridge repositioned (annotation #5), it stopped while oil was released (annotation #6) and then resumed moving (annotation #7).

Figure 34 presents data from “Run 2”, which were collected while the Turbol system was running. During this trial, the bridge would briefly move while releasing oil, then stop. This pattern repeated three times (see annotations).

The results shown in Figure 35 were obtained while the bridge was stationary and HOOPS oil was being injected, while a handheld wand was used to inject air bubbles as well. See annotations in Figure 35 for detail.

In Table 7, the results from the acoustically-obtained volume backscattering strength (Sv) are compared to the results for Sv obtained via LISST measurement in conjunction with the backscatter model for a fluid-filled sphere. Results for 'Run #2' (the data shown in Figure 34) are compared at each frequency and for each of the three oil releases that were performed during this run. These results are compared against the LISST/fluid-filled sphere model computations, and against computations that would have resulted if the LISST had produced estimates of N_v that were 100 times larger. Additionally, differences are computed between the Sv levels across different frequency pairings, and these differences are against compared against differences obtained using LISST data in conjunction with the fluid-filled sphere model for backscattering cross section.

4.3.2 Optical (LISST, fluorescence)

LISST data for the simulated oil releases suggest a high degree of dispersion for the Hoop Crude oil. The LISST was positioned within the plume during 5 distinct time periods during the releases. Total Particle Concentration maximum ranged between 7.8 – 25.1 ul/L. Data were normalized by the maximum value in order to visualize the Droplet Size Distribution (DSD) shape. Runs with the lowest and highest median droplet diameter are depicted in Figure 36 (run 1 and 3 represents the DSD at approximately 08:17 and 08:33 hours respectively, on 07-27-18). Smaller droplets remain in suspension longer than larger droplets, with 70-100 um serving as an operational definition of 'good' dispersion.

Fluorescence time series data were collected via the ROV-mounted UviLux and the EXO sonde, where the former was closest to the source of the plume release in the tank on 07-26-18 from 11:30 to 12:15 hours. Both sensors crossed the plume footprint four times, as evident from the peak values in the time series (Figure 37). Fluorescence estimates of oil concentration and timing of peak detection vary due to differing placement of sensors in the tank.

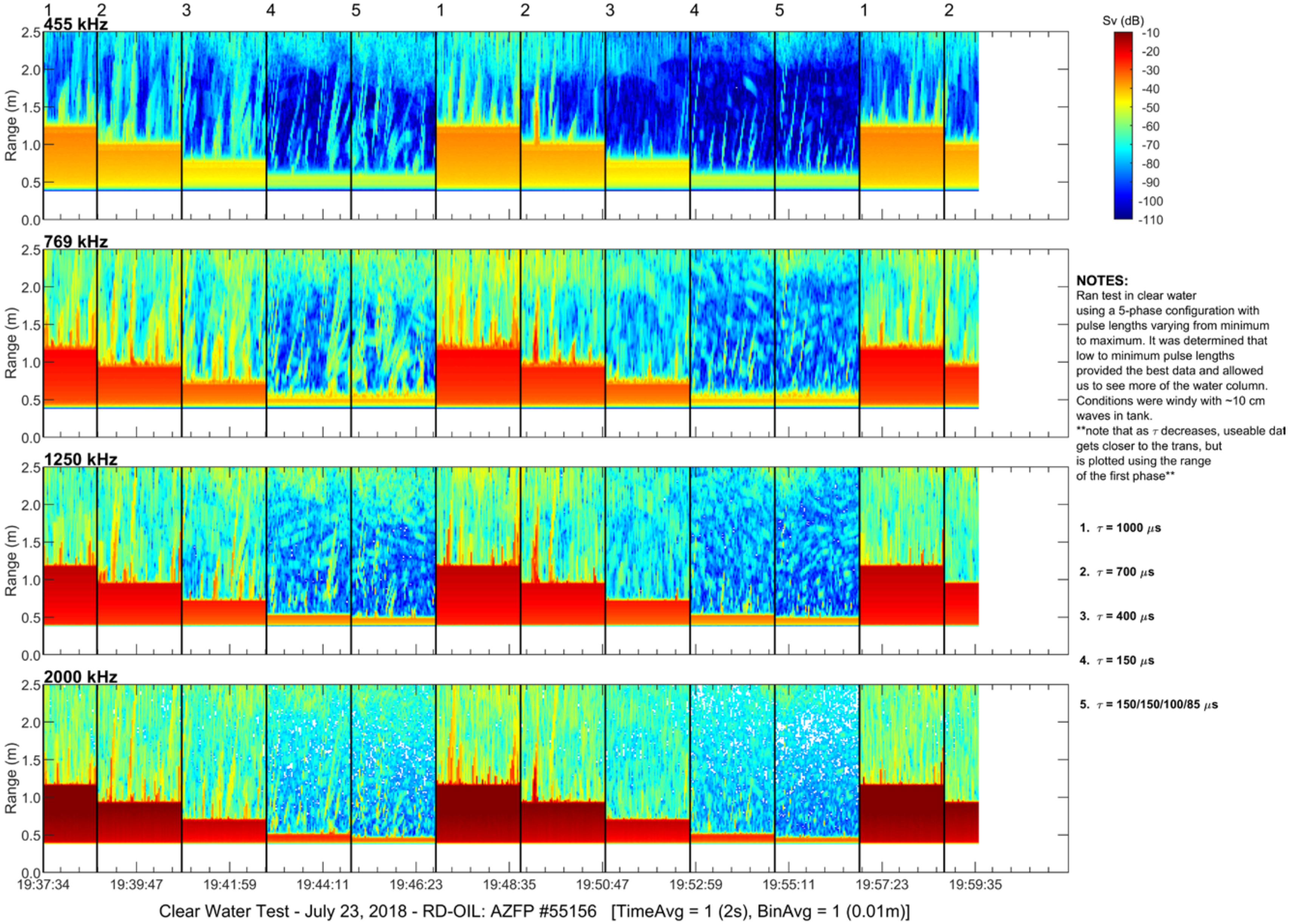

NOTES:
Ran test in clear water using a 5-phase configuration with pulse lengths varying from minimum to maximum. It was determined that low to minimum pulse lengths provided the best data and allowed us to see more of the water column. Conditions were windy with ~10 cm waves in tank.
note that as τ decreases, useable dat gets closer to the trans, but is plotted using the range of the first phase

1. τ = 1000 μs
2. τ = 700 μs
3. τ = 400 μs
4. τ = 150 μs
5. τ = 150/150/100/85 μs

Figure 31: Computed volume backscatter strength Sv (dB ref. 1/m) for the four AZFP frequencies during the Clear Water test on July 23, 2018.

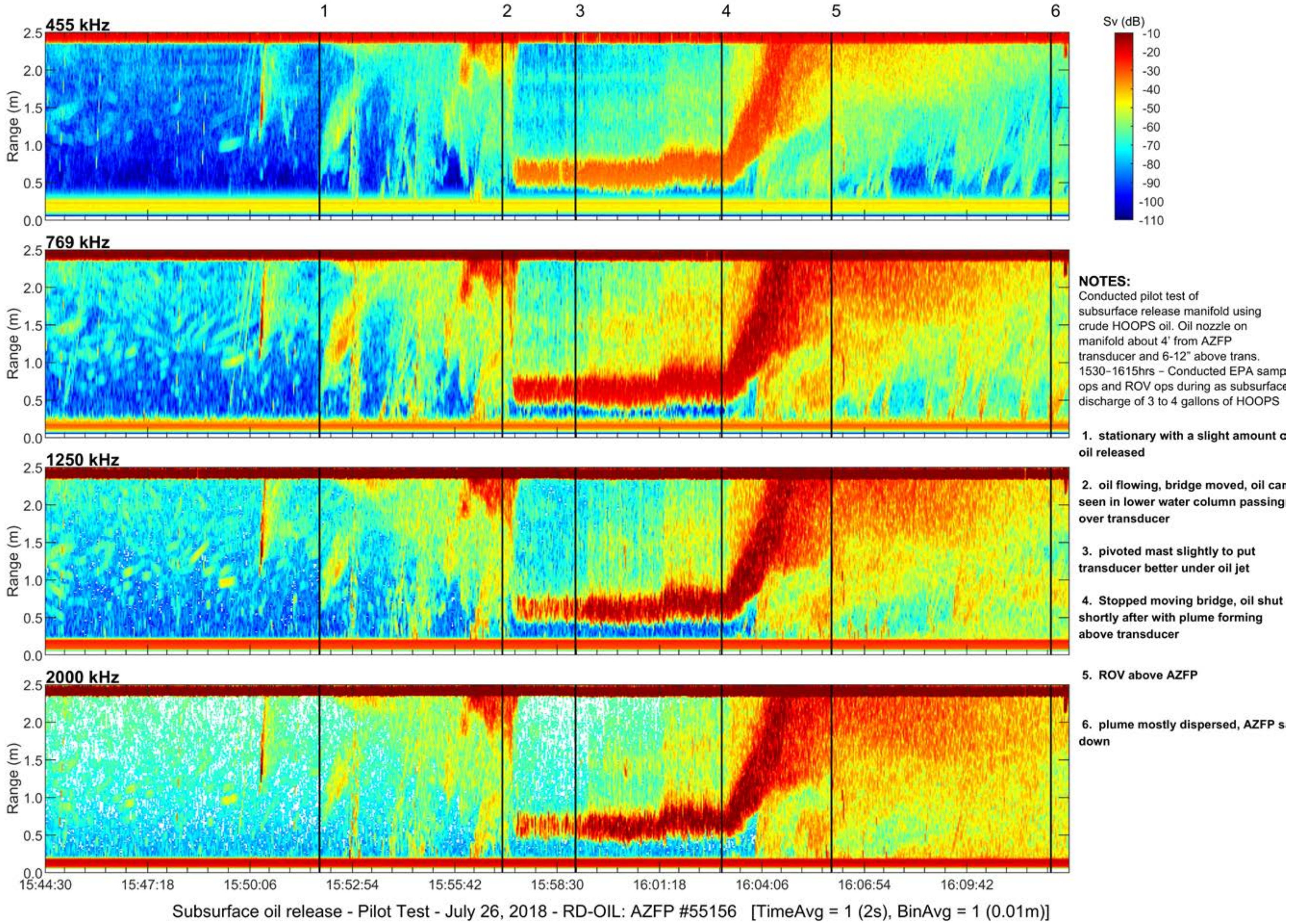

NOTES:
Conducted pilot test of subsurface release manifold using crude HOOPS oil. Oil nozzle on manifold about 4' from AZFP transducer and 6-12" above trans. 1530-1615hrs – Conducted EPA samp ops and ROV ops during as subsurface discharge of 3 to 4 gallons of HOOPS

1. stationary with a slight amount c oil released

2. oil flowing, bridge moved, oil car seen in lower water column passing over transducer

3. pivoted mast slightly to put transducer better under oil jet

4. Stopped moving bridge, oil shut shortly after with plume forming above transducer

5. ROV above AZFP

6. plume mostly dispersed, AZFP s down

Figure 32: Computed volume backscatter strength Sv (dB ref. 1/m) for the four AZFP frequencies during the Pilot test of the subsurface oil release on July 26, 2018.

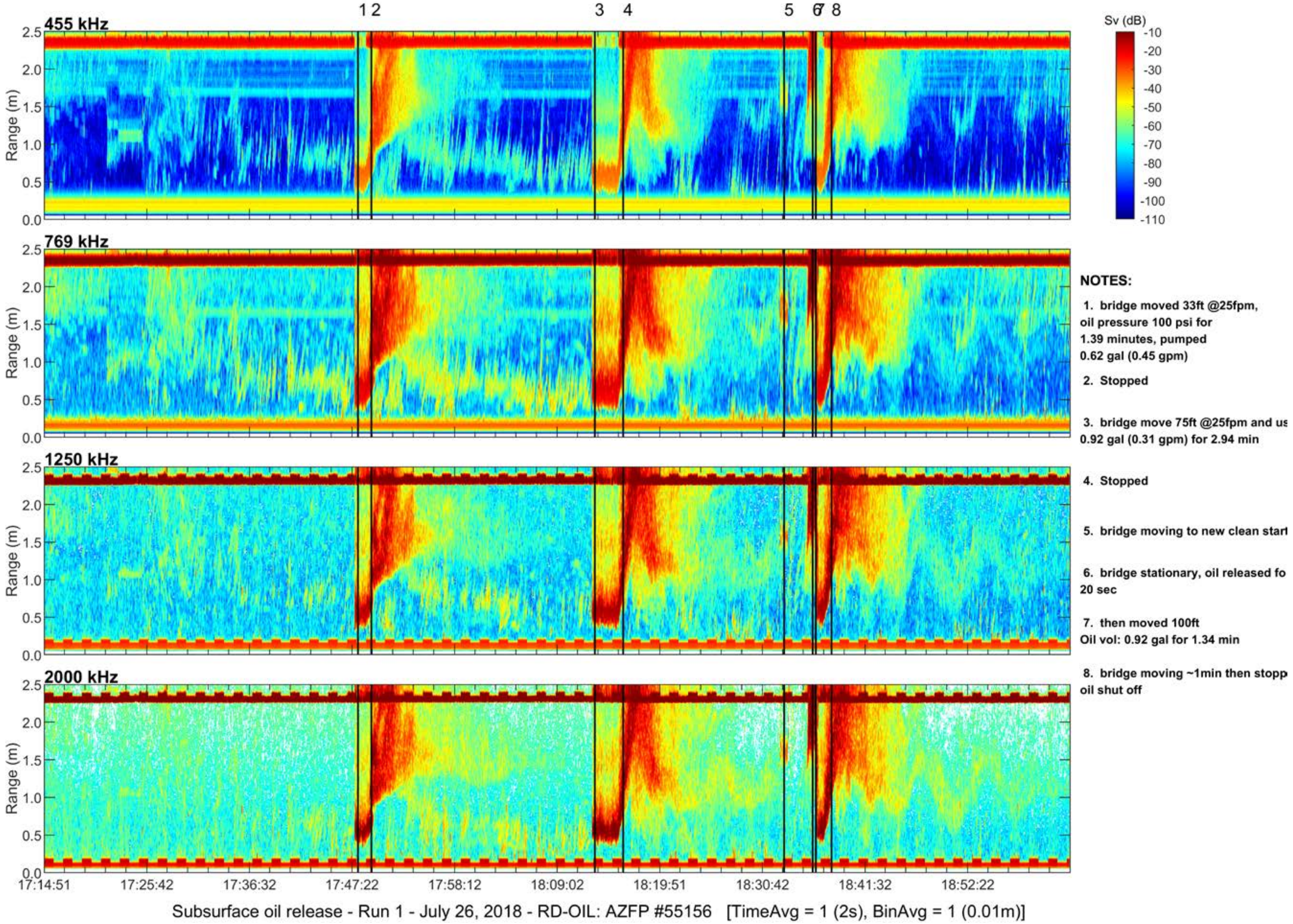

NOTES:

1. bridge moved 33ft @25fpm, oil pressure 100 psi for 1.39 minutes, pumped 0.62 gal (0.45 gpm)
2. Stopped
3. bridge move 75ft @25fpm and us 0.92 gal (0.31 gpm) for 2.94 min
4. Stopped
5. bridge moving to new clean start
6. bridge stationary, oil released fo 20 sec
7. then moved 100ft Oil vol: 0.92 gal for 1.34 min
8. bridge moving ~1min then stopp oil shut off

Figure 33: Computed volume backscatter strength Sv (dB ref. 1/m) for the four AZFP frequencies during the Run #1 of the subsurface oil release on July 26, 2018.

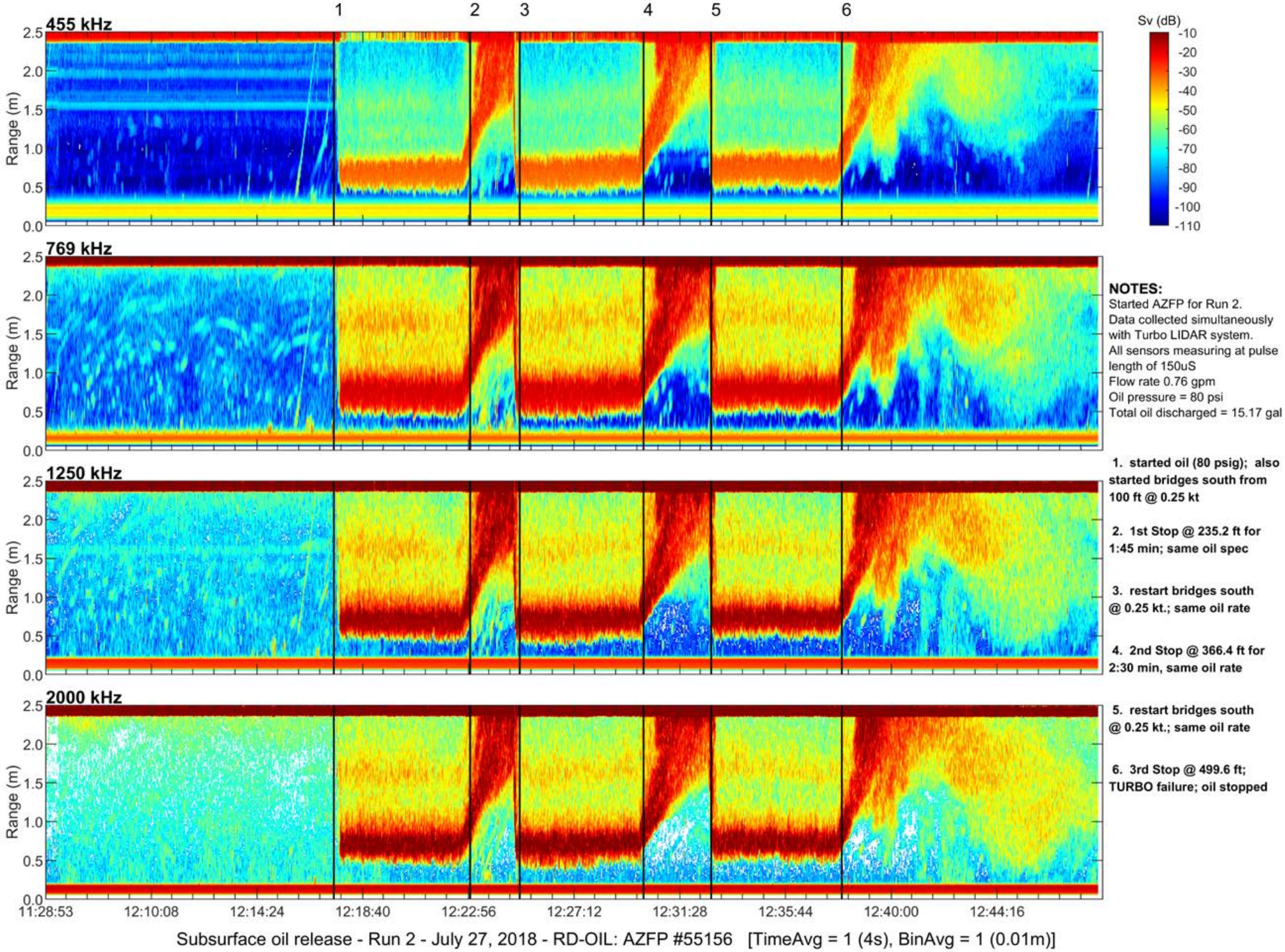

NOTES:
Started AZFP for Run 2.
Data collected simultaneously with Turbo LIDAR system.
All sensors measuring at pulse length of 150uS
Flow rate 0.76 gpm
Oil pressure = 80 psi
Total oil discharged = 15.17 gal

1. **started oil (80 psig); also started bridges south from 100 ft @ 0.25 kt**
2. **1st Stop @ 235.2 ft for 1:45 min; same oil spec**
3. **restart bridges south @ 0.25 kt.; same oil rate**
4. **2nd Stop @ 366.4 ft for 2:30 min, same oil rate**
5. **restart bridges south @ 0.25 kt.; same oil rate**
6. **3rd Stop @ 499.6 ft; TURBO failure; oil stopped**

Figure 34: Computed volume backscatter strength Sv (dB ref. 1/m) for the four AZFP frequencies during the Run #2 of the subsurface oil release on July 27, 2018.

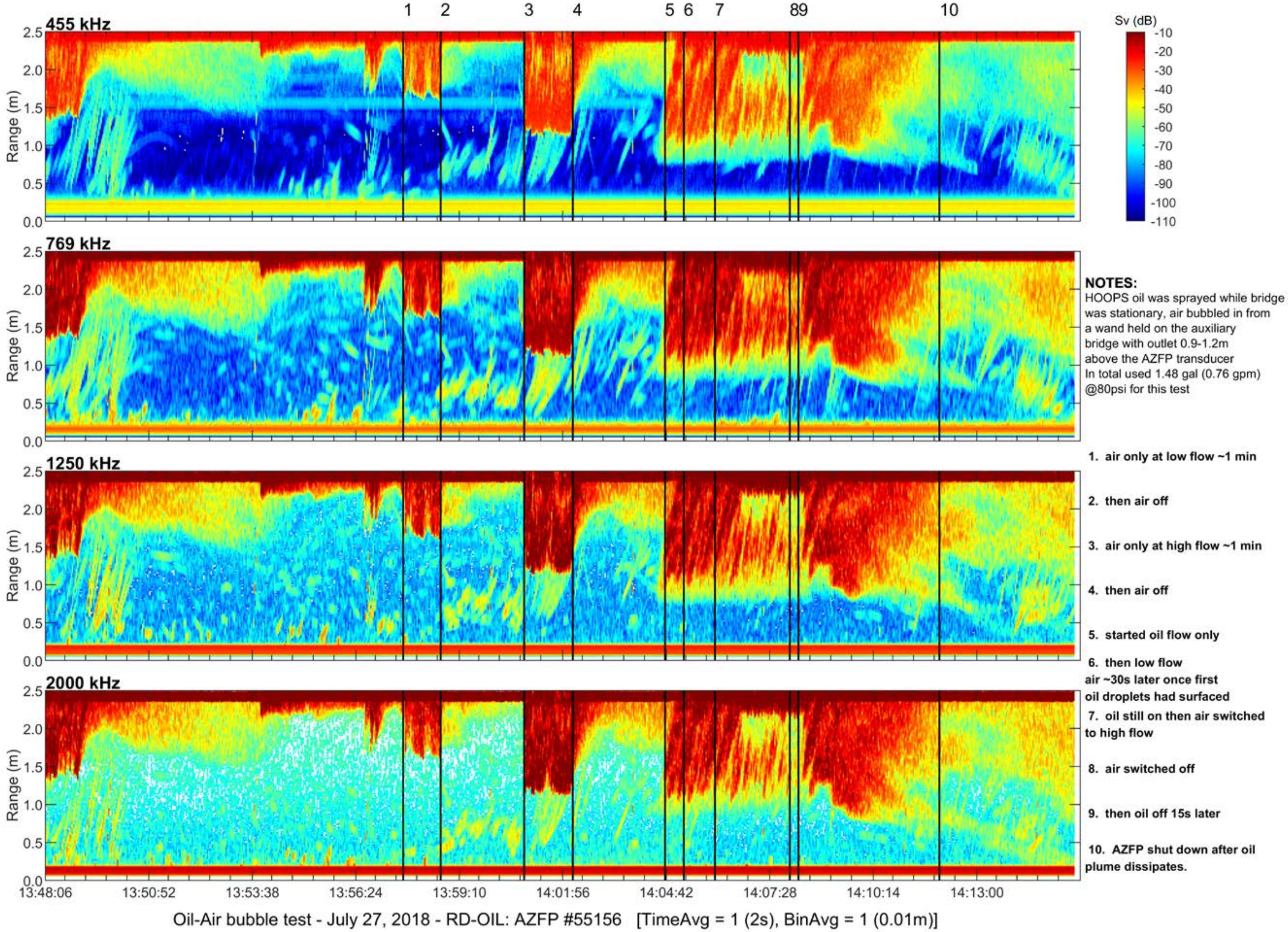

NOTES:
HOOPS oil was sprayed while bridge was stationary, air bubbled in from a wand held on the auxiliary bridge with outlet 0.9-1.2m above the AZFP transducer
In total used 1.48 gal (0.76 gpm) @80psi for this test

1. **air only at low flow ~1 min**
2. **then air off**
3. **air only at high flow ~1 min**
4. **then air off**
5. **started oil flow only**
6. **then low flow air ~30s later once first oil droplets had surfaced**
7. **oil still on then air switched to high flow**
8. **air switched off**
9. **then oil off 15s later**
10. **AZFP shut down after oil plume dissipates.**

Figure 35: Computed volume backscatter strength Sv (dB ref. 1/m) for the four AZFP frequencies during the Oil-Air Bubble Test of the subsurface oil release on July 27, 2018.

Table 7: Volume backscatter Sv (dB ref. 1/m) estimated using a fluid sphere model and measured using an AZFP (top) and differences between the four frequencies (455, 769, 1250, 2000 kHz).

			Sv (dB)			
	Oil Release #	**Title**	**Ch1 (455kHz)**	**Ch2 (769kHz)**	**Ch3 (1250kHz)**	**Ch4 (2000kHz)**
Run 2		Fluid Sphere Model	-53.1	-44.1	-36.1	-29.0
	1	AZFP measured	-33.1	-20.3	-14.5	-10.5
	2	AZFP measured	-32.5	-19.3	-14.2	-10.0
	3	AZFP measured	-31.6	-18.5	-14.7	-12.1
		Fluid Sphere Model (N*100)	-33.1	-24.1	-16.1	-9.0

	Oil Release #	Title	Ch2-1	Ch3-1	Ch4-1	Ch3-2	Ch4-2	Ch4-3
Run 2		Fluid Sphere Model	9.0	17.0	24.1	8.0	15.1	7.1
	1	AZFP measured	12.8	18.6	22.6	5.7	9.7	4.0
	2	AZFP measured	13.1	18.3	22.4	5.1	9.3	4.2
	3	AZFP measured	13.0	16.9	19.5	3.9	6.5	2.6

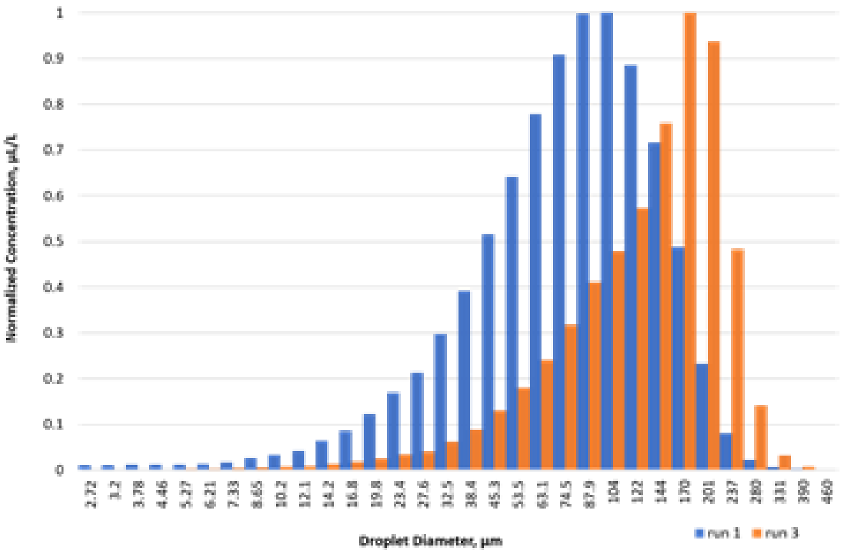

Figure 36. LISST Droplet Size Distribution of simulated plume of Hoops Crude oil.

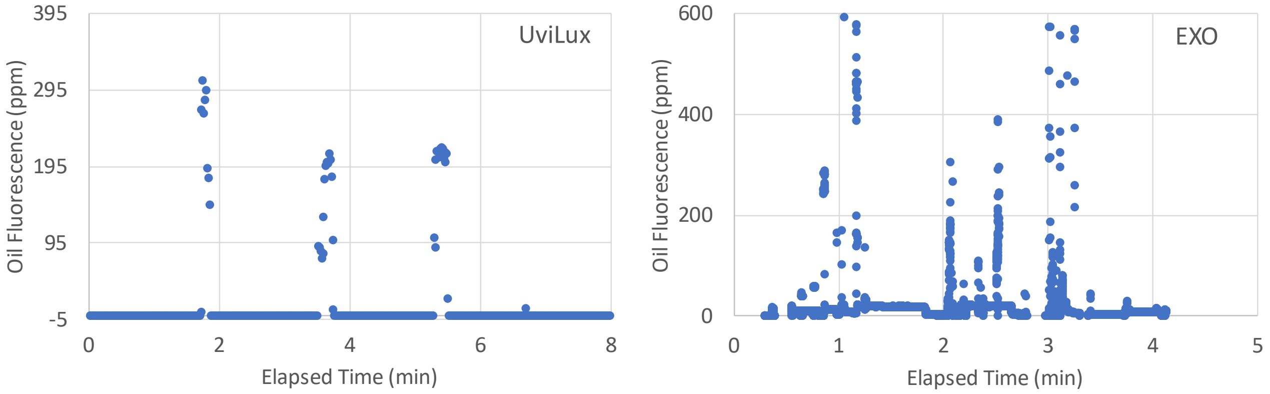

Figure 37. Oil fluorescence time series for simulated plumes in the tank.

4.3.3 Chemical (hydrocarbon analyses)

The plume samples from the test release at 11:30 am Local time on 07-26-18 were analyzed for TPH, PAH and alkanes (Table 8 and Figure 38 and 39). While the ROV autosampler volume was lower, the analyte concentration is higher due to a more targeted sample collection. The oil plume sample is predominantly composed of mid-length straight chain alkanes and naphthalenes. Since the sampling was instantaneous, early dissolution and evaporation process are minimal.

Table 8. Result Summary of Hydrocarbon Analysis

SAMPLE NAME	TPH (mg/L)	Total Alkanes (µg/L)	Total PAHs (µg/L)	BTEX (ng/mL)
Tank Blank	0.65	0.86	0.08	2041
NISKIN	0.62	8.24	5.39	42898
ROV	2.03	60.68	83.39	1129318

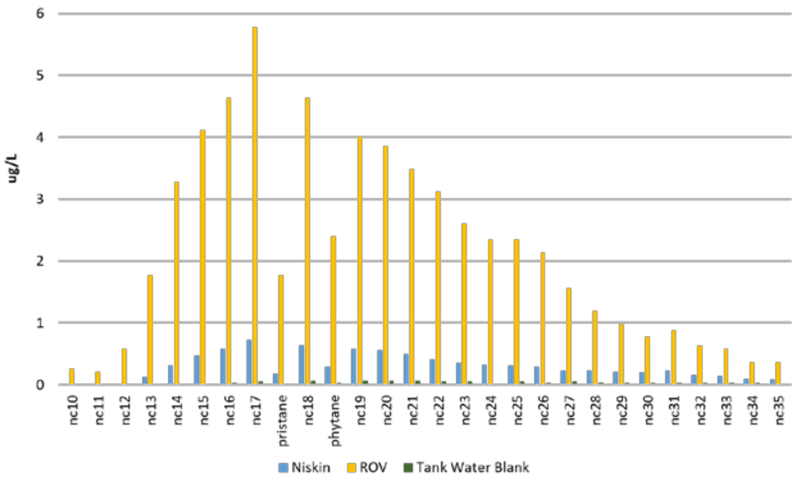

Figure 38. Alkanes in Hoops Crude oil jet release.

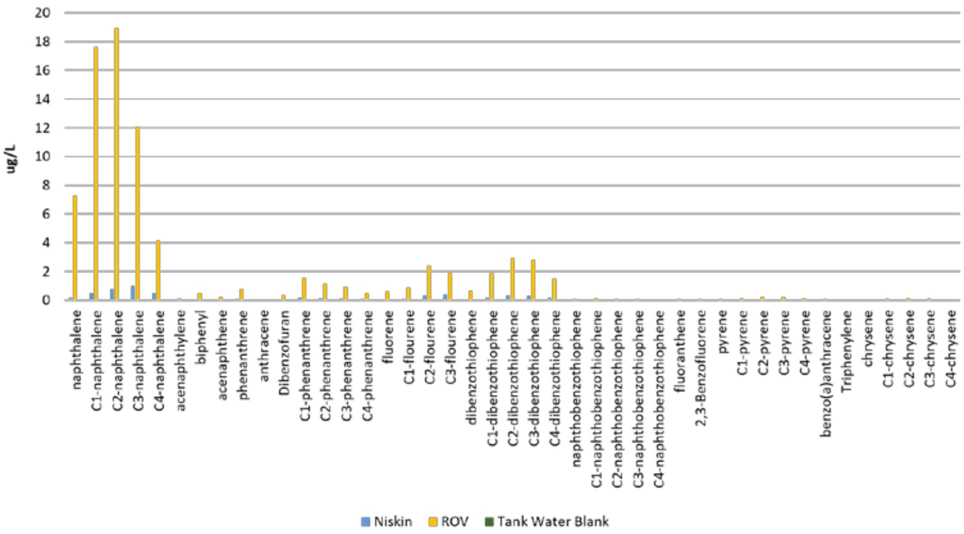

Figure 39. PAH compounds in Hoops Crude oil jet release.

4.4 Aerial and Underwater Imagery

We used the thermal and visible imagery from the UAV to create temperature and oil thickness estimates for each of the surface grid cells.

4.4.1 Aerial (UAV) Imagery

Figure 40A shows the irregular temperature distribution in each of the grid cells derived from the thermal emissivity imagery, and Figure 40B shows a false color image derived from the multispectral imaging system. Note the different appearance of crude oil cells (black) compared to the oil/water emulsion cells (reddish-brown). Figure 41 shows the oil thickness classification for each grid cell.

4.4.2 Underwater (ROV) Imagery

A link to the underwater video collected by the ROV can be found here: https://www.youtube.com/watch?v=Z3_h1_Jjmjw

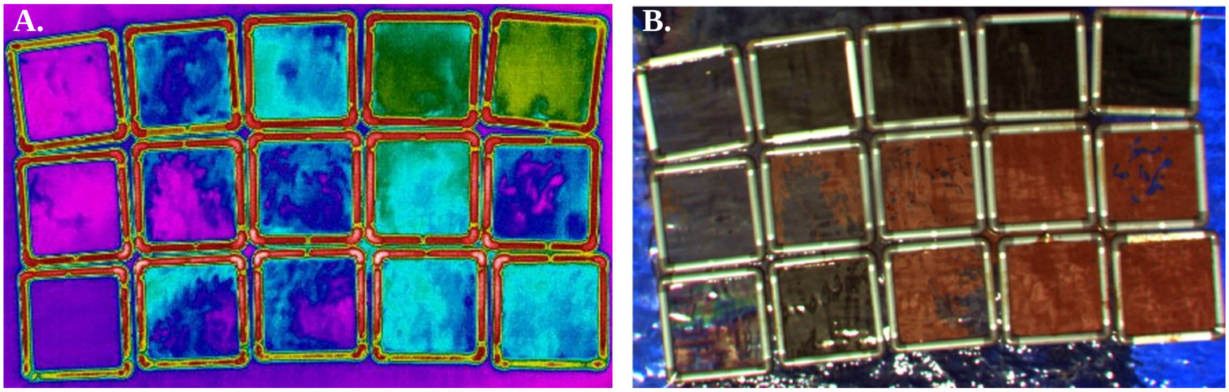

Figure 40. A. Temperature image of all grid cells. B. False color image of the grid cells (R:840; G:668; B:560 nm). Grid cell orientation in both panels as in Figure 13B.

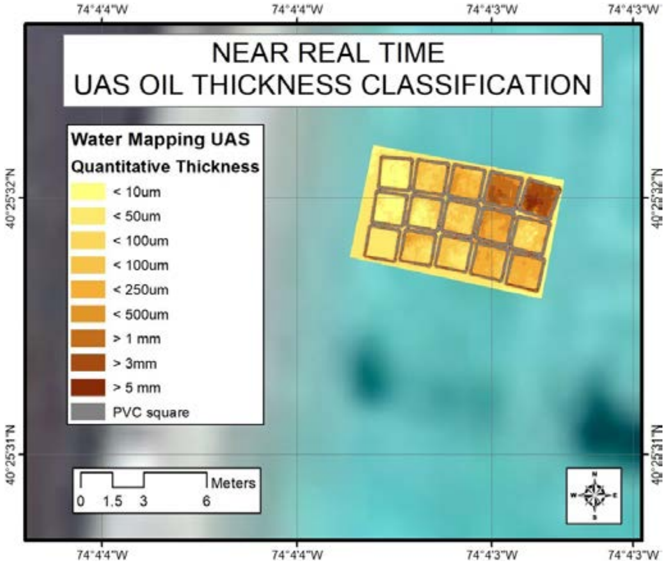

Figure 41. Oil Thickness classification for each grid cell.

5. DISCUSSION

LiDAR

Based on the results presented in section 4, the LiDAR capabilities for oil thickness estimates can be summarized as:

- The LiDAR can penetrate oil slick up to a thickness of 3 mm ± 1 mm
- The LiDAR optical depth measurement relates to the oil thickness. The relationship seems to allow to resolve fine scales from 0 to 1 mm and then lose sensitivity over 1 mm. The uncertainty and sensitivity threshold would require more research to be fully determined.
- Fluorescence can unambiguously detect oil slick. Even a non-optimal system based on a 532 nm laser (low quantum efficiency) and off-the shelf filter is fully functional.
- Fluorescence seems to relate to oil thickness. The fluorescence to oil thickness relationship does not seem to saturate in the millimiter range, contrary to non LiDAR sensors (ROW) and LiDAR elastic scattering.
- Both elastic scattering and fluorescence allow to determine the vertical structure of underwater oil plumes. Fluorescence should allow to discriminate between oil and other underwater features (phytoplankton, bubbles)
    - There is no ambiguity on the depth of the top of the oil plume (within the LiDAR vertical resolution uncertainty). The LiDAR should always be able to provide this information within its penetration range (10-30 m typical, up to 70 m claimed by some systems in some conditions).
    - The determination of the bottom altitude seems possible and may have been achieved during this work. It would require the use of another dedicated experiment to confirm this fact.

A key long term goal related to this experiment would be to determine if there is a design for a LiDAR system that could be deployed in the field in the event of an oil spill and help BSEE measure the flux or total volume of oil released in the ocean.

It is therefore important to understand than when the LiDAR estimates an oil thickness, it also estimates a volume. This is illustrated on Fig. 42. The LiDAR measures a small volume within a cone or cylinder created by the laser light. The vertical extent of this volume is the LiDAR vertical resolution (Table 2). For both SLOP and TURBOL, we estimate that the laser footprint diameter is around 20 cm. This value is related to eye safety requirements but is relatively easy to adjust on each individual systems. For this experiment, we assume homogeneity within a larger area (1 square meter grid) and the volume estimates were not the primary goal of this experiment, however the LiDAR is intrinsically measuring a volume of oil.

In section 4, we have discussed how the LiDAR backscatter signal from the bottom of the tank can be used to derive the optical thickness of the oil for both surface oil slick and subsurface oil release. This optical thickness measurement seems to relate to oil thickness through a bijective function. Although there's some limitation in the accuracy of the optical thickness to oil thickness relationship we determined, there is little ambiguity left that the relationship exist and it would be relatively straightforward to refine it with another dedicated experiment.

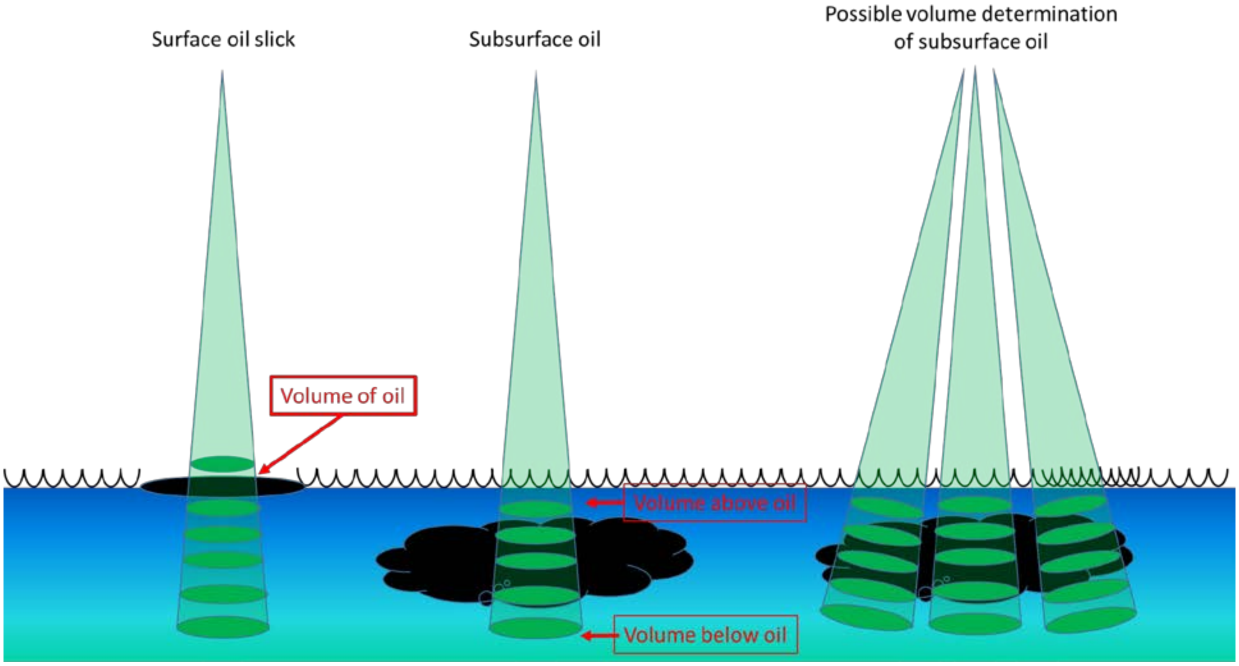

Figure 42. Schematic of different LiDAR measurements for surface and subsurface oil releases.

In the field, it would be difficult to use the bottom of the ocean, except in very well characterized littoral areas. The relationship we have determined would however still be valid. There are two ways to use this relationship in the field.

1) For surface oil slick, it is likely that we have to use the inversion of the LiDAR signal and determine the LiDAR ratio (Eq. 6) in order to estimate the optical depth from the backscatter measurements. As we can see on Fig. 43, there is a large variability of the LiDAR ratio between the different grid samples. Interestingly, there is not much difference between the 1mm and 2mm samples and it would definitely be important to perform more grid measurements to know if there is a natural variability of the oil LiDAR ratio or if we are reaching the limits of oil penetration and the optical depth measurement saturates. Note that the measurements shown on Fig. 43 should be considered relative to each other, to determine their absolute value, we would need to calibrate the LiDAR ocean signal on the atmospheric part of the profile. This is straightforward to do (CALIPSO level 1 ATBD, Hostetler 2006) but it is not part of the standard SLOP calibration procedure.

$$S_{oil} = \frac{1-e^{-2\tau_{oil}}}{2\int_{z_{surface}}^{z_{bottom}} \beta_{oil}(z)dz} \qquad (6)$$

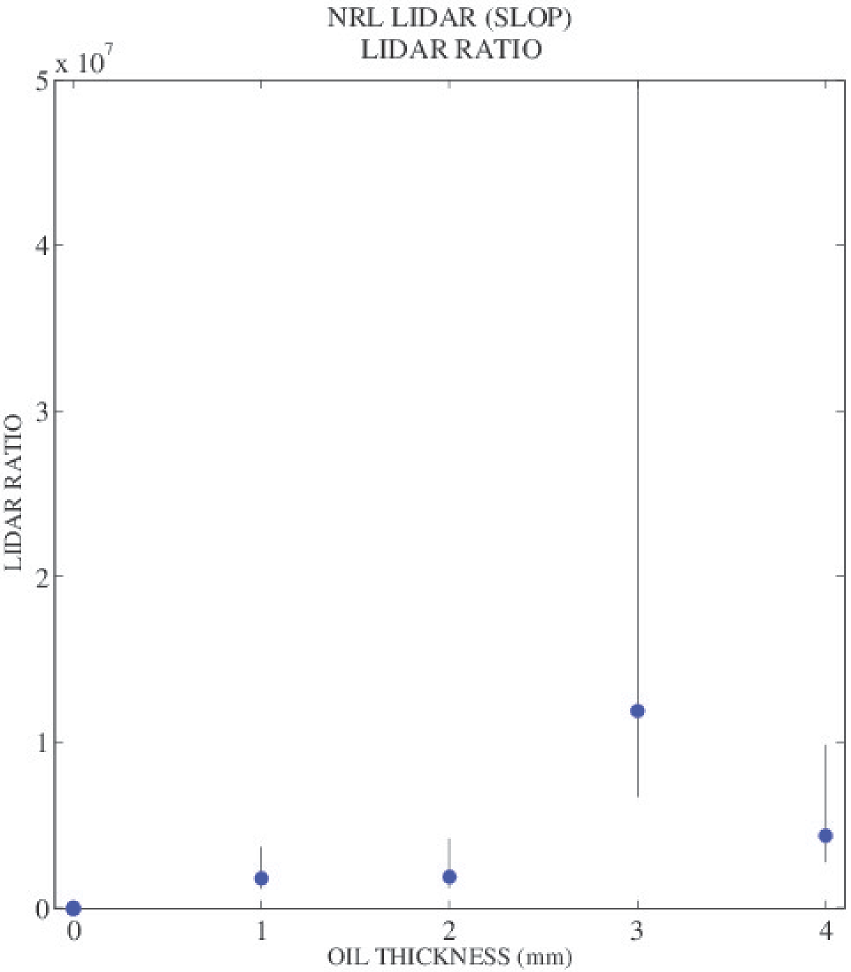

Figure 43. LiDAR ratio retrieval from the grid data (similar to Fig. 15 but for a different parameter).

2) A. In theory, it should be possible to only use the LiDAR signal under the oil slick as it corresponds to molecular water which is attenuated mainly by the presence of the oil slick. The preliminary analysis we conducted were not as conclusive as using the bottom of the tank and that is the reason why we did not present these results. There is a large difference of signal to noise ratio (one to two order of magnitudes) between the return of the bottom of the tank and the molecular return so it is not totally surprising that we would require a much larger statistic of calibration targets prior to be able to demonstrate this capability.

   B. For the subsurface release, it has been well demonstrated in the atmosphere that we can use the ratio of molecular scattering above and below the oil plume (central part of Fig. 42) to estimate the optical depth. This is more accurate than using only the bottom of the plume as using the ratio of two section of the same profile corrects any issue of attenuation in the water as well as calibration. As for the previous methodology, we have been lacking a sufficient sample to demonstrate this capability. However, as the only limitation of this methodology is the signal to noise ratio, even if for some reason SLOP could not do it, it is within reach of a specifically designed LiDAR system.

There are also two ways for the LiDAR to determine oil volume from elastic backscatter. The first one we just mentioned is to use the optical depth to determine oil thickness in the millimeter range. The second one is related to underwater oil release when the oil plume is much larger and mixed with water, in the cm range. In that case, the LiDAR signal will show the structure of the oil or at least the top of the oil layer. A scanning LiDAR like illustrated on the right part of Fig. 42 would be able to determine the 3 dimensional structure of oil (volume). A fast scanning system would provide a 4 dimensional view of the oil structure and be a direct measure of the oil flux. It is conceptually doable, especially for a system that would combine fluorescence and elastic scattering. However, more research needs to be conducted to confirm and strengthen several of the finding of this study.

NON LiDAR

For the above-water fluorescence measurements with the ROW instrument, fluorescence vs. oil thickness calibration curves were developed both in the laboratory and at Ohmsett. These two calibrations led to two quite different results, in terms of oil thickness vs. fluorescence signal. In addition, the laboratory calibration was performed at much finer resolution of oil thicknesses than was possible at Ohmsett; oil was added dropwise to a much smaller tank (a clean, plastic garbage can). However, due to the variable nature of fluorescence, which is based on oil type, age, measurement distance above the sample, and illumination conditions, we believe that a calibration performed at the same time under similar, natural solar illumination conditions is likely more appropriate. Thus, the Ohmsett calibration should be used, bearing in mind that the estimation of the reference oil thicknesses in the cells is likely not strictly correct, due to the uneven oil dispersal in the cells, as mentioned before.

To estimate the thickness of the oil accumulating on the surface during the subsurface oil release on 27 July, we therefore suggest that Figure 29B should provide a more accurate estimate (as opposed to Figure 29A which was derived using the laboratory calibration), up to a thickness of about 1mm, above which the non-linear fluorescence response does not permit adequate estimation. However, without independent oil thickness measurements, it is not possible to definitively say which calibration curve is more accurate.

Previous work has shown that thermal contrasts between oiled and non-oiled surfaces can provide an indication of oil thickness (Svejkovsky et al. 2012), however care must be taken using thermal contrast, because thermal differences can arise for many reasons, including upwelling flows, convergence zones, river outflows, and frontal zones (different water masses) (Leifer et al., 2012). In addition, day/night thermal patterns differ and depend on oil thickness, with thicker oiled surface temperatures showing higher values than those of surrounding non-oiled water surfaces during the day, and lower values at night (Svejkovsky et al. 2009). Nevertheless, our results do indicate that under the daylight sampling conditions in the tank at Ohmsett, we can estimate oil thicknesses from the thermal contrasts (Figures 30A and B), for crude and emulsified oils, respectively. The oiled surfaces exhibit higher temperatures than non-oiled surfaces, and the temperature difference for the crude oil is greater than for emulsified oils at the same thickness (however, there are not enough data points for the crude oil samples to draw definitive conclusions). A non-linear response was observed for the emulsified oil samples (Figure 30B).

For the acoustics, Figure 31 shows significant returns, even for short pulse lengths. Conditions on this day (July 23rd) were windy, and there were waves in the (shallow) tank. The backscatter seen in Figure 31 is potentially due to air bubbles in the water from the wave action at the surface. Pulse lengths of 150 us were deemed adequate at such short ranges, and at the higher frequencies (1250 kHz and 2000 kHz) it was decided that pulses even shorter than 150 us may be adequate.

The initial release of oil (Figure 32) was easily detected. Prior to the oil being released some anomalous backscatter was observed, but the backscatter from the oil is significantly stronger (signal-to-noise ratio of greater than 50 dB per channel). The oil plume observed during bridge motion is sharply defined (the horizontal 'line' at each frequency between annotations #2 and #4). The upward-looking AZFP was able to 'see' the surface of the water through the oil plume, at a range of approximately 2.5 m. When the bridge stopped moving, the upward motion of the oil droplets was observed as well (annotation #4).

Figure 33 shows data collected during three short releases of oil. Each channel of the AZFP shows some backscatter from the water column even before the oil was released. The origin of this backscatter is uncertain. However, when the oil is released it is clearly visible each time. As with Figure 32, ascending oil plumes are easily detected.

Figure 34 shows the data that were used in the comparison shown in Table 7. These data show a series of three oil releases that occurred during platform motion, followed each time by a stationary platform and a view of the plumes rising to the surface. As with other data, the oil release is clearly visible each time, as is the ascending plume. The plumes appear to broaden as the oil ascends, possibly a result of different droplet sizes having different rise rates. At a range of approximately 1.5 m is what appears to be a phantom target, likely a multipath return. It is interesting to note the downward trend in suspended oil that begins at approximately 12:42 UTC, after annotation #6.

Figure 35 shows strong scattering from both air bubbles and oil droplets, which are released at different times and from different locations during the experiment. Both the air bubbles and the oil are strongly visible. Future work at ASL will involve the application of scattering models (e.g. for air, and for oil droplets) to assess the extent to which air bubbles may be distinguished from oil droplets.

Table 7 presents results from a preliminary comparison between AZFP acoustically-obtained Sv estimates and Sv estimates obtained via the LISST in conjunction with an acoustical backscattering model. The Sv estimates produced by the LISST/backscatter model are significantly lower than those obtained by the AZFP. This discrepancy warrants further investigation, and its cause is presently unknown. One possible explanation is that a different model should have been selected for the acoustical backscatter cross section for the oil droplets. To assist with quantification of this discrepancy in Sv estimates, an arbitrary factor of one-hundred has been introduced into LISST estimates of the number of oil droplets present. Sv estimates that use the backscattering model are brought into close registration (with AZFP estimates of Sv) if the true number of droplets was one-hundred times greater than the true LISST estimates.

The collection of data (shown in Figures 31-34) show that oil in the water can be detected acoustically at all four frequencies used (455, 769, 1250 and 2000 kHz) by the AZFP. The largest absolute backscatter signals are at the highest frequencies. Initial results from an acoustic inversion (omitted from this report) indicate a median droplet size on the order of 100 um, consistent with the findings of Li and Garrett for oil in a turbulent natural environment (Li and Garrett 1998). This is perhaps a result of the turbulence of the jet used to inject the oil. The Signal-to-Noise Ratios are ~55, ~60, ~65, and ~65 dB for frequencies 455, 769, 1250 and 2000 kHz, respectively. This suggests that lower frequencies might also be effective in detecting oil in water, particularly if the droplets are larger.

6. LESSONS LEARNED

In terms of overall considerations, we believe a longer experiment would have been beneficial (2 weeks vs. 1 week). This would have allowed adequate set-up and tear-down times for all the equipment, and would allow for possible weather delays. A full-day of set-up was required for the LiDAR systems, which cut into the experiment/measurement times, and over a half day was required for tear-down and packing, and to ensure the tank was cleaned-up and ready for occupancy by another team the following week. Thus, only a little over 3 days were left for experimentation. There were also issues that affected the power supply to the LiDAR systems (power stability) that could have been explored and rectified if more time was available. For example, the power supply was not sufficiently continuous and uninterrupted; we discovered bridge movement resulted in power issues that caused the LiDARs to shut down.

For the LiDAR measurements, the 1m x 1m grid cells arranged in a 5x3 matrix with different oil concentrations (thicknesses) in each cell was not optimal. The small grid cells did not allow both LiDARs to shoot the same grid cell simultaneously. Also, the LiDARs were in a fixed position and could not be moved on the bridge, so moving the grid cell matrix on the water surface beneath the LiDARs was time consuming and cumbersome. A better arrangement would have been to use just a single grid cell that was large enough for both LiDARs to measure it simultaneously (perhaps 2m x 2m would have been adequate). This would mitigate the problem of moving the smaller grid cells back and forth and up and down in the tank. In addition, this arrangement would allow us to start with a low volume in the single, larger cell and sequentially add additional small volumes to gradually increase the oil thickness in finer increments. Thus, we could have measured a more finely-resolved series of oil thicknesses for multiple oil types and emulsions, rather than just the limited set that was done for just a few thicknesses.

We could use a more accurate way of determining where the laser was hitting the water surface, and thus the spot size of the target illuminated (rather than just geometric considerations). For example, some sort of combined camera system with imagery visible to the operator in real-time would help us better assess variable oil thicknesses measured by the LiDAR systems (to help estimate thickness uncertainties). Furthermore, *in situ* measurements of oil thickness in the grid cells would also help us better determine the reference thicknesses for the corresponding LiDAR measurements (perhaps using absorbant pads or glass slides), although uneven oil distribution within the cells could still be a problem. To mitigate the uneven oil distributions, smaller grid cells could be used, but this would be contrary to the larger sizes required for simultaneous measurements with both LiDARs, as discussed above.

For the acoustics, the AZFP data show that the subsea oil releases were easily detected by the AZFP at each of the four frequencies. The oil is seen to be a very strong target, with SNRs of greater than 50 dB were observed for each channel on the AZFP. It is speculated that these plumes could have been detected by the AZFP at far greater ranges than ~2 m because of the strength of the acoustical backscatter.

The data also indicate that future developments of the AZFP's oil detection capabilities should focus on new processing methods that enable the discrimination of oil from other targets such as air. As part of this effort a comprehensive search of available literature should be performed to facilitate the choice of scattering models for oil droplets in water, and also to inform the anticipated volume backscattering levels at each frequency.

7. RECOMMENDATIONS AND FUTURE WORK

For the LiDAR sampling protocol, we believe the instruments settings we used were adequate for this work to detect oil. There are a few things we might do to improve performance, such as changing the digitizer for the first bin of SLOP, and moving the power meter of TURBOL to improve fluorescence calibration (although fluorescence calibration is difficult, as these systems were not designed for that application). In terms of the power stability, Ohmsett was the first time we have had any issues (we have deployed both systems onboard ships, without power problems). If we were to deploy the LiDARs on a ship or platform to monitor the Taylor oil seep, we would make sure that we have "clean" power and we would bring our own generator (that we know works) as a backup.

In terms of future LiDAR work, additional measurements with larger grid cells (perhaps 2m x 2m) would be beneficial (so we could shoot the same sample with both LiDARs simultaneously). In addition, more targets with measurements over a wider range of oil content at finer resolution would enable us to more accurately determine the thicknesses ranges we can discriminate. These measurements would also help us determine the applicability/utility of using polarization measurements to characterize oil at the surface and in the water column; the polarization data from this experiment were not adequate to draw conclusions. Also, additional subsurface release experiments with different oil types, flow rates, and discharge scenarios would be useful, to better constrain the operational conditions suitable for LiDAR deployment.

The reflectance measurements from the LiDAR show promise as well for estimating oil thickness, but additional measurements with coincident hyperspectral radiometers at visible and SWIR wavelengths would improve calibration and characterization efforts. Although we did collect these measurements during this experiment over both of these spectral ranges using two field radiometers, the signal:noise measurements of the SWIR reflectances were not sufficient for this purpose (due to an instrument issue), and the visible reflectances appeared erroneous and not clearly interpretable (might also have been related to the erroneous oil thickness estimates in the reference cells).

In terms of the acoustics, subsequent oil detection experiments with the AZFP should focus on long-range detection of subsea oil. One of the primary advantages of using acoustics to detect subsea oil is that acoustics offer the potential to detect the oil at significantly greater ranges than other techniques (e.g. optics, mass spectrometry). Accordingly, effort should focus on assessing and developing the comparative strengths of the AZFP over alternative methods. In particular, subsequent experiments should assess the AZFP's oil detection performance at lower frequencies (e.g. 125 kHz, 200 kHz) and at longer range (e.g. 10 m, 20 m, 50 m). Future experiments at the Ohmsett facility would be desirable as part of this effort. In the future, it would be beneficial to conduct experiments featuring different (and larger) nozzle sizes such that the size of the oil droplets is increased. Experiments such as this could help to determine the droplet sizes that are clearly resolvable by the AZFP at each frequency. Additionally, it would be desirable to conduct experiments in deeper water (e.g. 10 m depth), where there is less concern about air bubbles or surface effects influencing the processing.

Subsequent research and development efforts with the AZFP should focus on developing the target identification capabilities of the system. Initial results with acoustical inversion methods warrant further investigation and are omitted from this report. As part of this development, research into acoustical backscattering models for oil droplets in water (as a function of frequency and droplet size) will be performed. The output from these models will then be used as a ground truthing for AZFP data processing.

An ambitious development of the AZFP as a tool to detect oil in water would be the development of a mission-specific AZFP configuration that is mounted on an underwater vehicle such as a Slocum glider. One possible vision of this technology would be that the AZFP is used not as a tool for definitive identification of the oil, but as a tool to identify oil-like anomalies at long range. Once the AZFP indicates the detection of an oil-like anomaly, the mission profile of the glider could be adjusted so that the glider flies near or through the anomaly and is then able to sample it with shorter-range sensors that can perform the definitive classification.

8. SUMMARY

We collected an extensive suite of LiDAR, optical, acoustic, and chemical measurements of surface oil slicks and subsurface plumes during a 1-week experiment at the Ohmsett Test Facility in July 2018. Analyses reveal that LiDAR remote sensing can detect and measure the presence of oil at the surface or underwater. LiDAR can retrieve a wide range of oil thicknesses, from a few microns up to several mm thick. This experiment did not provide enough data to know the minimal sensitivity but the resolution of the elastic scattering seems to increase for low (micron) oil thicknesses. Fluorescence provides an unambiguous signature of the presence of oil. In addition, estimates of volume detection and flux measurement seems possible with a specifically designed system.

For the acoustics, the AZFP detected the subsurface release of oil at all four frequencies, and the signal-to-noise ratio for these oil releases was in excess of 50 dB for each AZFP channel.

Initial results from this experiment indicate that the oil is clearly detectable by the AZFP, and that longer-range detection is likely possible. However, more work is needed in order to be able to discriminate oil from other targets such as air bubbles. The measurements of absolute acoustical backscatter from the AZFP facilitate the use of acoustical inversion techniques that may be able not only to discriminate oil from other targets, but also to characterize the oil (e.g. median droplet size). ASL is hopeful that in the future, funding may be secured which will facilitate this development effort.

9. ACKNOWLEDGMENTS

This research was supported by funding from BSEE (Dr. Jay Cho, Program Manager). We thank ASL Environmental Sciences Inc. for providing corporate support (time, salary costs) for technicians and scientists to collect and analyze the acoustic data sets (BSEE provided travel funds for ASL participation at Ohmsett). Mr. Alan Guarino and the staff at the Ohmsett Test Tank Facility provided excellent experimental support, and their efforts to ensure a successful experiment are gratefully acknowledged. Dr. Robert Grosser and Dr. Devi Sundaravadivelu (Pegasus Technical Services) performed the chemical analyses on the water samples.

10. REFERENCES

Anderson, V. 1950. Sound scattering from a fluid sphere. J Acoust. Soc. Am. **22**: 426-431.

Brekke, C., and A. H. S. Solberg. 2005. Oil spill detection by satellite remote sensing. Remote Sensing of Environment **95:** 1-13.

Carrera, P., J. Churnside, G. Boyra, V. Marques, C. Scalabrin, and A. Uriarte. 2006. Comparison of airborne lidar with echosounders: a case study in the coastal Atlantic waters of southern Europe. ICES Journal of Marine Science: Journal du Conseil **63:** 1736-1750.

Chave, R, J. Buermans, D. Lemon, C. DeCollibus, J.C. Taylor, G. K. Saba, C. Lembke, and C.S. Reiss, “Adapting Multi-frequency Echo-sounders for Operation on Autonomous Vehicles”, in Proceedings of MTS/IEEE OCEANS’18, Charleston, SC, 2018.

Churnside, J., B. McCarty, and X. Lu. 2013. Subsurface Ocean Signals from an Orbiting Polarization Lidar. Remote Sensing **5:** 3457-3475.

Churnside, J. H. 2014. Review of profiling oceanographic lidar. Opt Eng **53:** 1-13.

Churnside, J. H., and P. L. Donaghay. 2009. Thin scattering layers observed by airborne lidar. Ices J Mar Sci **66:** 778-789.

Fingas, M. 2018. The Challenges of Remotely Measuring Oil Slick Thickness. Remote Sensing **10:** 319.

Fingas, M., and C. Brown. 2014. Review of oil spill remote sensing. Marine pollution bulletin **83:** 9-23.

Hollinger, J., and R. Mennella. 1973. Oil spills: measurements of their distributions and volumes by multifrequency microwave radiometry. Science **181:** 54-56.

Hostetler, C. A., Liu, Z., Reagan, J., Vaughan, M., Winker, D., Osborn, M., Hunt, W. H., Powell, K. A., and Trepte, C.: CALIOP Algorithm Theoretical Basis Document, Calibration and Level 1 Data Products, PC-SCI-201, NASA Langley Research Center, Hampton, VA 23681, 66 pp., available at: http://www-calipso. larc.nasa.gov/resources/project_documentation.php, 2006.

Hornstein, N. 1973. The Visibility of Oil-Water Discharges. International Oil Spill Conference Proceedings **1973:** 91-99.

Hu, C. and others 2018. Remote sensing estimation of surface oil volume during the 2010 Deepwater Horizon oil blowout in the Gulf of Mexico: scaling up AVIRIS observations with MODIS measurements, p. 44. SPIE.

Kitamura, M., K. Amakasu, T. Kikuchi, and S. Nishino, "Seasonal Dynamics of Zooplankton in the Southern Chukchi Sea Revealed from Acoustic Backscattering Strength," Continental Shelf Research. **133** (1): 47-58, 2017.

Leifer, I. and others 2012. State of the art satellite and airborne marine oil spill remote sensing: Application to the BP Deepwater Horizon oil spill. Remote Sensing of Environment **124:** 185-209.

Lennon, M., S. Babichenko, N. Thomas, V. Mariette, G. Mercier, and A. Lisin. 2006. Detection and mapping of oil slicks in the sea by combined use of hyperspectral imagery and laser induced fluorescence. EARSeL eProceedings **5:** 120-128.

Lennon, M., N. Thomas, V. Mariette, S. Babichenko, and G. Mercier. 2005. Oil slick detection and characterization by satellite and airborne sensors: experimental results with SAR, hyperspectral and lidar data, p. 4 pp., Proceedings. 2005 IEEE International Geoscience and Remote Sensing Symposium, 2005. IGARSS'05. IEEE.

Panetta, P.D., D. McElhone, L. Carr, K. Winfield, G.G. Cartwright, and C.T. Friedrichs, "Final Report: Acoustic Assessment of Subsea Chemical Dispersant Efficacy", Project #1002, Bureau of Safety and Environmental Enforcement, Herndon, VA, 2014.

Sawada, K., T. Mukai, Y. Fukada, and T. Matsuura, "Comparison of Zooplankton Density Estimated by Acoustic Inversion Method and Net Sampling," Journal of the Acoustical Society of America, **140** (4): 3242-3243, 2016.

Sun Z Q, Zhao Y S, Yan G Q, et al. Study on the hyperspectral polarized reflection characteristics of oil slicks on sea surfaces. Chinese Sci Bull, 2011, 56: 1596−1602, doi: 10.1007/s11434-010-4112-5

Svejkovsky, J., M. Hess, J. Muskat, T. J. Nedwed, J. McCall, and O. Garcia. 2016. Characterization of surface oil thickness distribution patterns observed during the Deepwater Horizon (MC-252) oil spill with aerial and satellite remote sensing. Marine pollution bulletin **110:** 162-176.

Svejkovsky, J., W. Lehr, J. Muskat, G. Graettinger, and J. Mullin. 2012. Operational Utilization of Aerial Multispectral Remote Sensing during Oil Spill Response. Photogrammetric Engineering & Remote Sensing **78:** 1089-1102.

Svejkovsky, J., J. Muskat, and J. Mullin. 2009. Adding a multispectral aerial system to the oil spill response arsenal. Sea Technology **50:** 17-22.

Zielinski, O., T. Hengstermann, D. Mach, P. Wagner, A. Steinhage, and C. Winkel. 2001. Multispectral information in operational marine pollution monitoring: A data fusion approach. 5th International Airborne Remote Sensing Conference.